Catalysis Letters (2023) 153:1–18
https://doi.org/10.1007/s10562-022-03961-0

Kinetic Parameter Estimation for Catalytic H_2–D_2 Exchange on Pd

Nicholas Golio[1] · Irem Sen[1] · Zhitao Guo[1] · Rucha Railkar[1] · Andrew J. Gellman[1,2]

Received: 6 February 2022 / Accepted: 13 February 2022 / Published online: 15 March 2022

Abstract

Kinetic parameters have been estimated for the H_2–D_2 exchange reaction on a thin film Pd catalyst by fitting reaction data from T = 333 to 593 K over a range of inlet partial pressures, $P^{in}_{H_2}$ and $P^{in}_{D_2}$. A rigorous approach to estimating the 95% confidence regions of the kinetic parameters reveals some of the issues and complexities that are not routinely considered in the estimation of kinetic parameter uncertainty from catalytic data. Three different mechanistic models were used to assess the influence of subsurface hydrogen, H′: the traditional Langmuir–Hinshelwood (LH) mechanism, the Single Subsurface Hydrogen (1H′) mechanism, and the Dual Subsurface Hydrogen (2H′) mechanism. The fitting was performed by fixing the pre-exponential factors for all Arrhenius rate constants and equilibrium constants to their transition state theory values. The diffusion of H and D atoms from the surface into the subsurface was constrained to be endothermic (i.e. $\Delta E_{ss} > 0$) and represented as an equilibrium process. Performance of the fitting routine was evaluated on a noiseless simulated dataset (created using $\Delta E^{\ddagger}_{ads} = 0$, $\Delta E^{\ddagger}_{des} = 43$, and $\Delta E_{ss} = 25$ kJ/mol) and the same simulated dataset with the inclusion of 3% Gaussian noise. In both cases, the solver was able to return the chosen values of $\Delta E^{\ddagger}_{ads}$, $\Delta E^{\ddagger}_{des}$, and ΔE_{ss}. Mapping of the behavior of the residual sum of squared errors, χ^2, about its global minimum within 3D (ϵ_{ads}, ϵ_{des}, ϵ_{ss}) parameter space allowed quantification and visualization of the 95% confidence regions using 2D error ellipses for each pair of fitting parameters. For the experimental dataset on the Pd catalyst, fitting to the LH model predicted that H_2–D_2 exchange is adsorption rate limited, with $\Delta E^{\ddagger}_{ads} = 51.1 \pm 0.6$ kJ/mol with 95% confidence. On the other hand, fitting to both the 1H′ and 2H′ models led to predictions of $\Delta E^{\ddagger}_{ads} = 0$, consistent with the current understanding that the barrier to H_2 dissociation on Pd is low. Thus, the results detailed herein provide supporting evidence for a non-LH mechanism for H_2–D_2 exchange on Pd while also illustrating the issues associated with quantification of uncertainty in kinetic parameter estimation.

Graphical Abstract

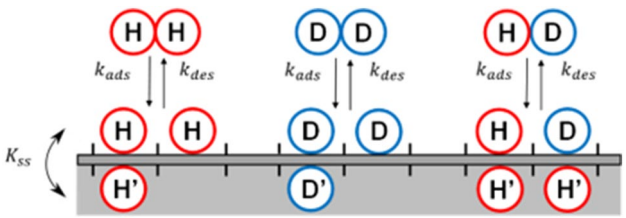

Keywords Catalysis · Palladium · H_2–D_2 exchange · Hydrogen adsorption · Kinetics · Uncertainty estimation · Parameter fitting

1 Introduction

Reactions involving H_2 have a wide range of industrial applications. For example, H_2 is used as a fuel in advanced energy systems, such as fuel cells [1–4], and it is also used for various catalytic hydrogenation reactions [5–8]. Because it is

✉ Andrew J. Gellman
gellman@cmu.edu

[1] Department of Chemical Engineering, Carnegie Mellon University, 5000 Forbes Ave, Pittsburgh, PA 15213, USA

[2] W.E. Scott Institute for Energy Innovation, Carnegie Mellon University, 5000 Forbes Ave, Pittsburgh, PA 15213, USA

often derived from fossil fuels, H_2 must be separated from CO_2-rich gas mixtures. Standard methods for H_2 separation and purification include solvent absorption, pressure swing adsorption, and cryogenic distillation, all of which require large capital and energy expenditures [9, 10]. Metal membrane filters offer a promising alternative for purifying H_2 due to their low operating cost and low energy consumption [11]. Pd-based membranes are commonly used for H_2 separation since they can easily dissociate H_2 and dissolve H atoms, and they have a high permeability for H atoms once dissolved [12]. Pd membranes also possess a high selectivity to H_2 transport relative to other gases [13, 14]. It has been shown that Pd or Pd-alloy membranes are stable for several months under H_2 flow in the temperature range 900–1046 K [15, 16]. However, there are limitations to using pure Pd membranes for H_2 purification. H_2 adsorption on Pd below its critical point of 571 K and 2 MPa produces both α-PdH and β-PdH phases, which have different lattice constants. Phase transitions between these two hydrides cause lattice strain and result in the formation of bulk and grain boundary defects [17]. Ultimately, H_2 embrittlement causes membrane rupture after repeated pressure and temperature cycling [18–20].

Transport of H_2 through Pd-based membranes involves five steps: dissociative adsorption of H_2 on the upstream side of the membrane surface to form H atoms, dissolution of H into the subsurface, diffusion of dissolved H atoms through the bulk, diffusion of subsurface H′ atoms to the downstream surface, and associative desorption of H_2 from the downstream surface [21, 22]. This transport process is known to be limited by the bulk diffusion of H atoms, as manifested by its half-order dependence, $n_{H_2} = 1/2$, on H_2 pressure, P_{H_2} [23]. Decreasing the membrane thickness increases the order of the hydrogen pressure dependence and increases the permeability through Ag-Pd alloys [18, 23, 24]. For ultrathin Ag-Pd alloy films with thicknesses < 500 nm, the H_2 transport is reported to be first-order, $n_{H_2} = 1$, in P_{H_2} over the temperature range 373–523 K [18]. This result indicates that surface reactions, i.e. the H_2 adsorption step at the upstream surface dictate the rate of hydrogen transport through ultrathin Ag-Pd membranes.

While the bulk diffusion of H atoms through Pd has been investigated extensively [25–27], the surface reactions of H_2 adsorption and desorption on Pd-based alloy surfaces are not as well understood. The kinetics of the H_2–D_2 exchange reaction ($H_2 + D_2 \rightarrow 2HD$) can provide valuable information about the adsorption and desorption steps [21, 22]. Hence, our estimation of the kinetic parameters associated with the H_2–D_2 exchange reaction on Pd provides important insight into hydrogen purification by Pd-based membranes. Understanding the kinetics of H_2 adsorption is also a fundamental component of understanding other surface reactions, such as catalytic hydrogenation, that involve adsorbed H atoms.

Numerous studies of H_2 on Pd surfaces have shown that it adsorbs with a negligible barrier to dissociation and a high heat of adsorption [28–30]. The most straightforward approach to modeling H_2–D_2 exchange on Pd involves application of the traditional Langmuir–Hinshelwood (LH) framework. H_2–D_2 exchange has the simplest possible surface reaction mechanism as described by the LH framework. The reaction mechanism is parametrized by just two rate constants: k_{ads} for the dissociative adsorption of H_2 and k_{des} for the associative desorption of H_2 (Fig. 1). However, the kinetic behavior predicted by the LH mechanism has been found to be inconsistent with several experimental observations of H_2–D_2 exchange on Pd catalysts. Savara et al. observed that on Pd(111) and Pd nanoparticles [31, 32] with $P_{D_2} \gg P_{H_2}$ and high total surface coverage, $\theta \cong 1$, the reaction order in P_{D_2} was $n_{D_2} = 0$. This differs from the LH prediction of $n_{D_2}^{LH} = -1$ for $P_{D_2} \gg P_{H_2}$ and high total surface

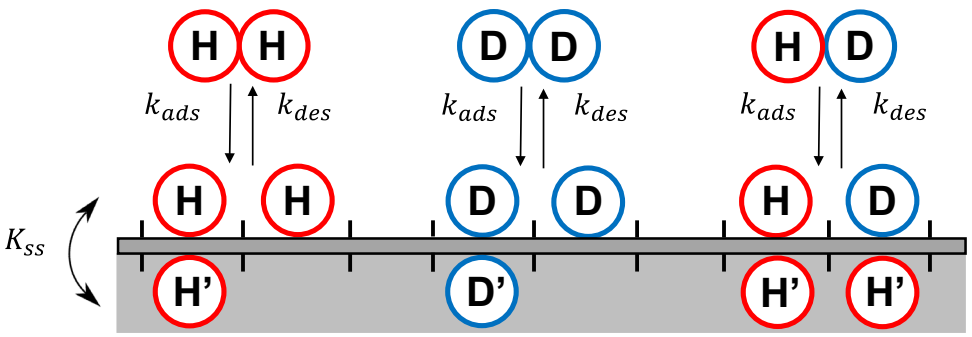

Fig. 1 Schematic diagram of the H_2–D_2 exchange reaction on a catalyst surface. H_2, D_2, and HD adsorb competitively on the catalyst surface into adjacent empty sites. All three have the same Langmuir–Hinshelwood adsorption and desorption rate constants, k_{ads} and k_{des}. The surface-to-subsurface diffusion equilibrium constant, K_{ss}, quantifies the equilibrium between adsorbed H and D atoms and absorbed H' and D' atoms in the immediate subsurface layer. Note that hydrogen adsorption and desorption can occur with zero, one, or two H' (or D') atoms in the immediate subsurface

coverage, $\theta \cong 1$. The LH prediction results from the intuition that the surface is already saturated with deuterium ($\theta_D \approx 1$) when $P_{D_2} \gg P_{H_2}$ thus, increasing P_{D_2} will inhibit H_2 adsorption, thereby decreasing θ_H. Similarly, Sen et al. observed that the H_2–D_2 exchange reaction order in P_{H_2} was $n_{H_2} = 0$ for $P_{H_2} \gg P_{D_2}$ and $\theta \cong 1$ using the same Pd catalyst film used for this work [33].

The importance of subsurface hydrogen, herein denoted by H′, has been increasingly documented in the field of heterogeneous catalysis [29, 31, 32, 34–38], and has the ability to explain deviations from the LH framework for H_2–D_2 exchange. Density functional theory (DFT) studies have shown that Pd is the only transition metal for which subsurface H′ atoms are energetically stable with respect to gaseous H_2 [36, 39]. Consequently, the contribution of subsurface H′ must be considered in order to accurately model the kinetics of catalytic reactions involving H_2 on Pd and Pd-based alloys. Previously, two H_2–D_2 exchange mechanisms were proposed, both of which include the presence of subsurface H′ (and D′) in the rate equations [33]. These mechanisms (Fig. 2), referred to as the Single Subsurface Hydrogen mechanism (1H′) and the Dual Subsurface Hydrogen mechanism (2H′), expand on the LH framework by allowing diffusion of surface H and D atoms into and out of the subsurface layer with an equilibrium constant, K_{ss} (Fig. 1). Fundamentally, the subsurface hydrogen mechanisms require the presence of either one or two adjacent H′ or D′ species in the immediate subsurface in order to facilitate the hydrogen adsorption and desorption processes occurring on the adjacent top surface sites. Analysis of these mechanisms under conditions where $P_{H_2} \gg P_{D_2}$ and $\theta \cong 1$ revealed that the Dual Subsurface Hydrogen mechanism (2H′) is consistent with the reaction order $n_{H_2} = 0$ observed in the earlier work using this Pd catalyst film [33].

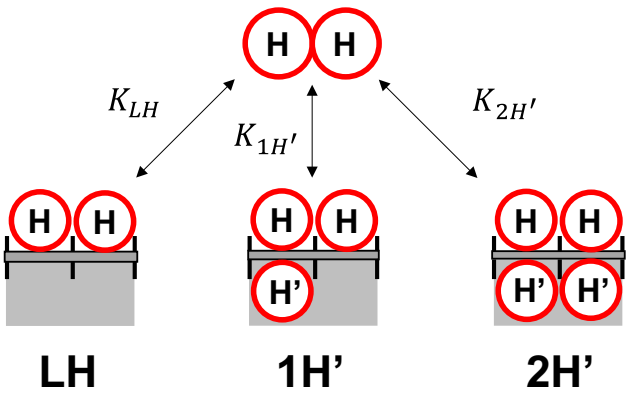

Fig. 2 Schematic representation of the three different reaction models investigated in this work. The Langmuir–Hinshelwood mechanism (LH) only involves adsorption and desorption from the top surface. In the Single Subsurface Hydrogen mechanism (1H'), an H' (or D') atom in the immediate subsurface layer influences the energetics of adsorption and desorption from the adjacent sites on the surface. In the Dual Subsurface Hydrogen mechanism (2H'), two adjacent H' (or D') atoms in the subsurface layer influence the energetics of adsorption and desorption from the adjacent sites on the surface

In this study, the catalytic kinetic data for H_2–D_2 exchange on the pure Pd region of a Ag_xPd_{1-x} composition spread alloy film [33] was used to estimate the fundamental kinetic parameters associated with three different mechanistic models: LH, 1H′, 2H′. A schematic illustration of each mechanism is presented in Fig. 2. The three kinetic parameters considered were the barriers to H_2 (D_2) adsorption and desorption, $\Delta E^{\ddagger}_{ads}$ and $\Delta E^{\ddagger}_{des}$, and the surface-to-subsurface H (D) transport energy, ΔE_{ss}. The uncertainty regions for each kinetic parameter were visualized using the Hessian matrix describing the curvature of the residual χ^2 at its optimal value (minimum) to reveal confidence limits on the parameter fitting results. The kinetics of H_2–D_2 exchange on Pd offers an interesting case study opportunity to explore the limits of kinetic parameter estimation for the three mechanisms: LH, 1H′, and 2H′. This is possible because we have developed analytic expressions for the three rate laws describing the exchange kinetics [33]. These rate laws enable us to rationalize some of the observations made during analysis of the reaction kinetics. In addition, we have applied the relevant methods to map out the statistical confidence regions across 3D parameter space spanned by ϵ_{ads}, ϵ_{des}, and ϵ_{ss}, in such a way that the limitations of these methods can be appreciated.

2 Experimental

The data analyzed herein are a subset of a larger dataset that includes the rates of H_2–D_2 exchange measured over a range of temperatures and inlet pressures of H_2 and D_2 on 90 compositions of Ag_xPd_{1-x} spanning the range $x = 0 \rightarrow 1$, as described earlier [33]. This was accomplished using a Ag-Pd composition spread alloy film (CSAF) and a multichannel microreactor array capable of isolating 100 regions of the CSAF, all having different alloy compositions [40, 41]. This study focuses on the methodology for extraction of confidence intervals for kinetic parameters derived from three models of the reaction mechanism. As such, we focus on the reaction rates for catalytic H_2–D_2 exchange obtained on the most Pd-rich region of the CSAF, which has a nominal composition of $Ag_{01}Pd_{99}$. Throughout, we refer to this simply as the Pd catalyst.

2.1 Measurements of H_2–D_2 Exchange Kinetics

The H_2–D_2 exchange activity of the Ag_xPd_{1-x} CSAF was measured at 90 different alloy compositions using a high-throughput 100-channel microreactor array which has been described in detail elsewhere [40]. Only 90 channels of the

reactor were in use because the inlet flow to one row of 10 reactors was blocked. Reactant mixtures of H_2, D_2, and Ar were delivered continuously to the 90 isolated regions of the Ag_xPd_{1-x} CSAF surface, and products were continuously withdrawn from each region for analysis using an Extrel quadrupole mass spectrometer.

The H_2–D_2 exchange activity of the Ag_xPd_{1-x} alloys contained on the CSAF was measured at atmospheric pressure and over a temperature range from $T = 333$ to 593 K. The H_2 inlet partial pressure spanned the range $P^{in}_{H_2} =$ 23–230 Torr and the D_2 inlet partial pressure spanned $P^{in}_{D_2} =$ 0.23–230 Torr with Ar constituting the remainder of the gas flow. The temperature was increased in 20 K increments from 333 to 593 K, and the reaction was allowed to reach steady-state by waiting for 4 min at each temperature before beginning the analysis of the product gases from each of the reactor channels. The composition of the reaction products was calculated by assuming that the mass spectrometer signals at $m/z = 2$, 3, and 4 amu obtained from the product gas samples were proportional to the H_2, HD, and D_2 partial pressures. Baseline (0% conversion) signals at $m/z = 2$, 3, and 4 amu were collected by sampling the feed gas mixture directly without it contacting the CSAF surface. The dataset collected from these measurements consists of the HD flow rate exiting each of the reactor channels measured over a range of: catalyst compositions, x; temperatures, T; and inlet pressures, $F^{out}_{HD}(x, T; P^{in}_{H_2}, P^{in}_{D_2})$. The subset of these data analyzed in this work are $F^{out}_{HD}(x = 0.01, T; P^{in}_{H_2}, P^{in}_{D_2})$; i.e. the data from the most Pd rich region of the CSAF.

3 Kinetic Parameter Estimation

3.1 The Dual-Subsurface Hydrogen (2H′) H_2–D_2 Exchange Mechanism

Several studies of H_2–D_2 exchange on Pd surfaces have provided evidence for a non-LH mechanism that involves both surface hydrogen atoms, herein denoted by H, and subsurface hydrogen atoms, herein denoted by H′ (Fig. 2) [31–33]. The primary kinetic evidence for a non-LH mechanism is that under conditions where $P^{in}_{H_2} \gg P^{in}_{D_2}$ and $\theta \approx 1$, the reaction order in $P^{in}_{H_2}$ is $n_{H_2} = 0$, whereas the LH mechanism predicts a reaction order of $n_{H_2} = -1$. Our comparison of several alternative mechanisms revealed one in which two adjacent subsurface H′ or D′ atoms in sites below two adjacent surface H or D atoms serve to facilitate associative desorption of the two surface atoms. A derivation of the rate law for the Dual-Subsurface Hydrogen (2H′) mechanism has been provided previously [33] and predicts a reaction order of $n_{H_2} = 0$ for $P^{in}_{H_2} \gg P^{in}_{D_2}$ and $\theta \approx 1$. In brief, an equilibrium constant for surface–subsurface diffusion (K_{ss}), as illustrated in Fig. 1, describes the equilibrium between adsorbed H or D atoms and absorbed H′ or D′ atoms in the immediate subsurface layer. The presence of subsurface species, H′ or D′, influences the dissociative adsorption and associative desorption kinetics on the surface, modifying the rate equation for H_2–D_2 exchange from that given by traditional LH kinetics. The overall rate of HD production given by the 2H′ mechanism is

$$r_{HD} = 2k^{2H'}_{des}\theta_H\theta_D\theta'^2 - k^{2H'}_{ads}P_{HD}(1-\theta)^2\theta'^2 \tag{1}$$

where $k^{2H'}_{ads}$ is the rate constant for dissociative adsorption of HD onto two adjacent empty surface sites with H′ or D′ in their immediate subsurface, and $k^{2H'}_{des}$ is the rate constant for associative desorption of HD from two adjacent filled surface sites with H′ or D′ in their immediate subsurface. Note that the rate constants for H_2, D_2, and HD adsorption (or desorption) are all taken to be equal (i.e. isotope effects causing zero-point energy differences are ignored). The quantity P_{HD} is the pressure of HD in the gas phase, and $\theta = \theta_H + \theta_D$ and $\theta' = \theta'_H + \theta'_D$ represent the fractional coverages of surface and subsurface hydrogen species, respectively. The equilibrium expressions for θ_H, θ_D, θ, and θ' given by the 2H′ mechanism can be found in Eqs. 2–5. In the following equations, $K_{2H'}$ represents the adsorption equilibrium constant given by the ratio $k^{2H'}_{ads}/k^{2H'}_{des}$.

$$\theta_H = \frac{K_{2H'}P^{in}_{H_2}}{K_{2H'}P^{tot}_H + \sqrt{K_{2H'}P^{tot}_H}} \tag{2}$$

$$\theta_D = \frac{K_{2H'}P^{in}_{D_2}}{K_{2H'}P^{tot}_H + \sqrt{K_{2H'}P^{tot}_H}} \tag{3}$$

$$\theta = \frac{K_{2H'}P^{tot}_H}{K_{2H'}P^{tot}_H + \sqrt{K_{2H'}P^{tot}_H}} \tag{4}$$

$$\theta' = \frac{K_{ss}K_{2H'}P^{tot}_H}{K_{ss}K_{2H'}P^{tot}_H + \sqrt{K_{2H'}P^{tot}_H}} \tag{5}$$

The quantity $P^{tot}_H = P^{in}_{H_2} + P^{in}_{D_2} = P_{H_2} + P_{HD} + P_{D_2}$ is the total pressure of hydrogen containing species in the gas phase and is constant at each point along the length of the reactor.

Note that the rate constant for HD formation and desorption, $k^{2H'}_{des}$, is multiplied by a factor of 2 in Eq. 1. This arises from the statistics of atomic collisions leading to a reaction with a rate constant $k^{2H'}_{des}$. In a mixture of H and D atoms, the total collision frequency is proportional to

$\left(\theta_H + \theta_D\right)^2 = \left(\theta_H^2 + 2\theta_H\theta_D + \theta_D^2\right)$. The coefficient of 2 on the $\theta_H\theta_D$ term describing H–D collision frequency has been used explicitly in Eq. 1 rather than embedding it into a new rate constant. The presence of this factor of 2 also ensures that the rate expression that we have used yields the correct equilibrium constant of $\left(P_{HD}^{eq}\right)^2/\left(P_{H2}^{eq}\right)\left(P_{D2}^{eq}\right) = 4$ at full conversion of the initial mixture of H_2 and D_2.

From the perspective of assessing our ability to perform accurate parameter estimation, one of the attractive features of this problem is the fact that one can find analytical rate laws for the LH, 1H′, and 2H′ mechanisms for H_2–D_2 exchange. The design equation for a catalytic surface reaction in a flow reactor relates the catalyst surface area, A, to a mass balance represented by the following integral [42].

$$A = \int_0^{F_{HD}^{out}} \frac{dF'}{r_{HD}} \tag{6}$$

The catalyst area, A, is known because we are using a thin film reactor area of $900 \times 700\ \mu m^2$. Solving the integral using the expression for r_{HD} in Eq. 1 and rearranging the result yields an expression for the molar outlet flow rate of HD ($F_{HD}^{2H'}$, mol/s) generated by the 2H′ mechanism in terms of kinetic parameters and experimental conditions.

$$F_{HD}^{2H'} = \frac{2k_{des}\theta_H\theta_D F^{tot}}{k_{ads}(1-\theta)^2 P^{tot}}\left[1 - \exp\left(-\frac{Ak_{ads}(1-\theta)^2\theta'^2 P^{tot}}{F^{tot}}\right)\right] \tag{7}$$

In Eq. 7, F^{tot} is the total molar flow rate through the reactor including the inert stream of Ar and P^{tot} is the total pressure inside the reactor (~ 1 atm).

The rate constants for adsorption and desorption are in the Arrhenius form, each parametrized by its pre-exponential factor, ν, and activation energy ($\Delta E^{\ddagger}$). Because the activation energy term lies inside an exponential, all analysis was done using the logarithm of the pre-exponents to balance the sensitivity of the fitting objective function, χ^2, to both parameters.

$$k_{ads} = \nu_{ads}\exp\left(-\frac{\Delta E_{ads}^{\ddagger}}{RT}\right) \tag{8}$$

$$k_{des} = \nu_{des}\exp\left(-\frac{\Delta E_{des}^{\ddagger}}{RT}\right) \tag{9}$$

In Eqs. 8 and 9, R is the ideal gas constant and T is the reaction temperature in K. The equilibrium constant for surface-subsurface diffusion, K_{ss}, is given by the ratio of the rate constant for surface-to-subsurface diffusion, $k_{s\to ss}$, and the rate constant for subsurface-to-surface diffusion, $k_{ss\to s}$.

$$K_{ss} = \frac{k_{s\to ss}}{k_{ss\to s}} = \frac{\nu_{s\to ss}\exp\left(-\frac{\Delta E_{s\to ss}^{\ddagger}}{RT}\right)}{\nu_{ss\to s}\exp\left(-\frac{\Delta E_{ss\to s}^{\ddagger}}{RT}\right)} = \nu_{ss}\exp\left(-\frac{\Delta E_{ss}}{RT}\right) \tag{10}$$

In Eq. 10, ν_{ss} represents the ratio of the pre-exponents for the two diffusion rate constants and $\Delta E_{ss} = \Delta E_{s\to ss}^{\ddagger} - \Delta E_{ss\to s}^{\ddagger}$ is the reaction energy for surface-to-subsurface transport of H and D atoms. When $\Delta E_{ss} > 0$, the transport of hydrogen from the surface into the subsurface layer is an endothermic process.

To summarize the data fitting problem briefly, the 2H′ model contains six kinetic parameters: three pre-exponential factors ($\log(\nu_{ads})$, $\log(\nu_{des})$, and $\log(\nu_{ss})$) and three energies ($\Delta E_{ads}^{\ddagger}$, $\Delta E_{des}^{\ddagger}$, and ΔE_{ss}). For a given mechanistic model, e.g. 2H′, the three pairs of ν and ΔE correspond to the rate constant for dissociative adsorption, $k_{ads}^{2H'}$, the rate constant for associative desorption, $k_{des}^{2H'}$, and the equilibrium constant for surface-subsurface diffusion, K_{ss}.

3.2 Parameter Estimation from a Noiseless Simulated Dataset

In order to assess the difficulty of fitting 6-parameter kinetic model proposed for the 2H′ mechanism to the kinetic data for H_2–D_2 exchange, a simulated dataset was generated for the 2H′ mechanism by assuming values for the three pairs of pre-exponential factors, ν, and energy terms, ΔE. Transition state theory was used to estimate reasonable values for the pre-exponents [43]. Assuming a mobile transition state, $\nu_{ads} = 10^2$ mol/m^2/s/Torr for dissociative adsorption and $\nu_{des} = 10^6$ mol/m^2/s for associative desorption. The pre-exponential factors for the surface–subsurface diffusion rate constants, $k_{s\to ss}$ and $k_{ss\to s}$, are assumed to be roughly equal to one another, resulting in $\nu_{ss} = 10^0$. The energy barriers used for creating the simulated data were chosen to be $\Delta E_{ads}^{\ddagger} = 0$ kJ/mol and $\Delta E_{des}^{\ddagger} = 43$ kJ/mol based on values for similar Pd-alloy systems [21] and the known values from fitting our data for Pd. An endothermic subsurface diffusion energy of $\Delta E_{ss} = 25$ kJ/mol is close to the value of 29 kJ/mol calculated in a DFT study of hydrogen absorption into pure Pd [29]. Using the fixed kinetic parameters defined above, a dataset was generated using Eq. 7 to calculate the HD molar flow rate at the outlet, $F_{HD}^{out}(T; P_{H_2}^{in}, P_{D_2}^{in})$, as a function of reaction temperature and the inlet partial pressures of H_2 and D_2. The reaction temperature was varied from $T = 333$ to 593 K in increments of 20 K, as done experimentally. The inlet H_2 pressure was varied from $P_{H_2}^{in} = 23$–230 Torr and the inlet D_2 pressure was varied from $P_{D_2}^{in} = 0.23$–230 Torr while keeping the total inlet flow rate constant at $F^{tot} = 2.5 \times 10^{-7}$ mol/sec/channel. In total, 14 different inlet flow conditions were simulated across the range of 14 reaction temperatures, yielding a data set of 196 points (partially

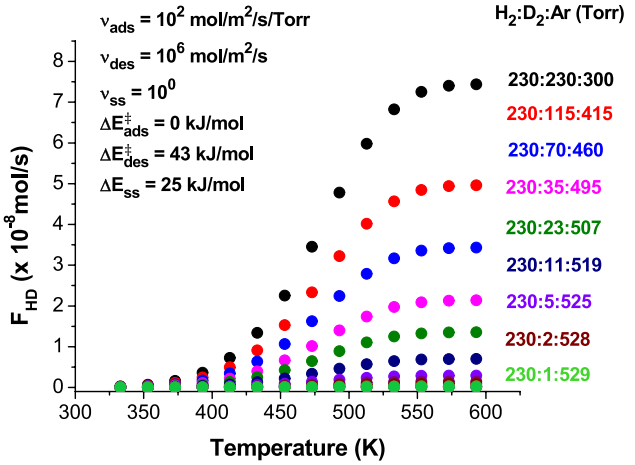

Fig. 3 Noiseless simulated data for the outlet molar flow rate of HD (F^{out}_{HD}) versus temperature as predicted by the 2H' mechanism, with $\nu_{ads} = 10^2$ mol/m^2/s/Torr, $\nu_{des} = 10^6$ mol/m^2/s, $\nu_{ss} = 10^0$, $\Delta E^{\ddagger}_{ads} = 0$ kJ/mol, $\Delta E^{\ddagger}_{des} = 43$ kJ/mol, and $\Delta E_{ss} = 25$ kJ/mol. All data points of the same color correspond to a particular inlet combination of $P^{in}_{H_2}$ and $P^{in}_{D_2}$ in Ar

shown in Fig. 3) representing the data for a Pd catalyst; $F^{out}_{HD}(T; P^{in}_{H_2}, P^{in}_{D_2})$. Figure 3 shows that the reaction conditions span the full range of conversions, with each curve achieving its equilibrium conversion at high temperatures.

The 2H′ rate law (Eq. 7) was fitted to the simulated data using the MATLAB® minimization tool *fmincon*, which is designed for constrained, nonlinear, multivariable functions. Other built-in MATLAB® solvers, such as *lsqcurvefit* and *nlfit*, were explored and found to perform equally well. Initially, all six kinetic parameters were fit to the simulated dataset using 1000 initial parameter guesses (seeds) spanning a wide range of parameter space. The pre-exponential factors of the initial seeds were varied over 10 orders of magnitude and the energy barriers were varied from 0 to 100 kJ/mol. Initializing the solver at 1000 different points explored the potential for the solver to find multiple minima, or not converge on a minimum at all. For each initial seed guess, the optimal kinetic parameters were estimated using the solver to sample parameter space and minimize an objective function which, in this case, is the relative sum of squared errors, χ^2, over all 196 data points. In order to give similar weights to the low and high conversion data points, the relative error between the fit and the simulated data points was used in the definition of χ^2 as shown in Eq. 11.

$$\chi^2 = \sum \left(\frac{F^{solv}_{HD} - F^{sim}_{HD}}{F^{sim}_{HD}} \right)^2 \tag{11}$$

F^{solv}_{HD} is the HD flow rate calculated by the solver as it samples parameter space and F^{sim}_{HD} is the HD flow rate calculated using the parameter values chosen for the simulated dataset. The parameter values that yielded the lowest value of χ^2 among the 1000 optimizations were chosen as the optimal solution; i.e. the best estimates of $\log(\nu_{ads})$, $\log(\nu_{des})$, $\log(\nu_{ss})$, $\Delta E^{\ddagger}_{ads}$, $\Delta E^{\ddagger}_{des}$, and ΔE_{ss}. Since the dataset contained no noise, the solver was able to converge to the exact solution with $\chi^2 < 3 \times 10^{-9}$ for ~ 25% of the 1000 iterations (initial seeds). In ~ 60% of the optimizations, the solver failed to move from the initial guess because the χ^2 function was flat across the local parameter space. This occurred when the combination of parameters used for the initial guess predicted either zero conversion or full conversion (the equilibrium flow rate) at all reaction temperatures and inlet flow conditions. In the remaining ~ 15% of iterations, the solver converged to various local minima with significantly higher values of $\chi^2 > 1$ than the one found at the optimum parameter set.

In order to understand the landscape of this (or any) parameter estimation problem and to extract some understanding of the confidence limits associated with an optimal fit, one needs to understand the full extent of $\chi^2\left(\vec{p}\right)$, where $\vec{p}$ represents a vector of the set of parameters over which the optimization is conducted. In this case, contour plots of χ^2 were generated for pairs of kinetic parameters to visualize their impact on χ^2 and on the quality of the fit. Particularly important are the contour plots for the pairs of kinetic parameters that define a single rate constant (i.e. $\log(\nu_{des})$ and $\Delta E^{\ddagger}_{des}$). Figure 4 shows χ^2 versus $\log(\nu_{des})$ and ϵ_{des} evaluated while holding the parameters determining k_{ads} and K_{ss}

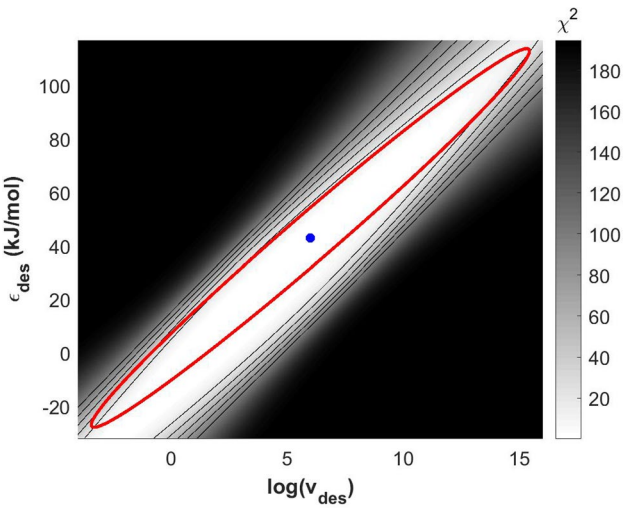

Fig. 4 Grayscale map and contour plot of χ^2 versus $\log(\nu_{des})$ and ϵ_{des} about the true minimum, marked by the blue dot at $\Delta E^{\ddagger}_{des} = 43$ kJ/mol and $log\left(\nu_{des}\right) = 6$. The values of χ^2 were calculated using the simulated data from Fig. 3 with no added noise. The red ellipse bounds the region of 95% confidence around the solution. Thus, any combination of points within the ellipse gives a reasonable fit to the simulated dataset

at their optimal values. For clarity, the symbols ϵ and ν used throughout this work represent parameter space generally, whereas the quantities ΔE and ν represent the values of the optimum fitted kinetic parameters. In other words, if ϵ_{des} is the variable spanning the range of desorption energy barriers, then $\Delta E^{\ddagger}_{des} = 43$ kJ/mol is the value of ϵ_{des} at the optimum fit to the simulated data. The value of this distinction will become apparent during the discussion of uncertainty estimation in Sect. 4. In Fig. 4, the solution point found by the solver (with $\chi^2 < 3\times10^{-9}$) is marked by the blue dot and falls exactly at the predefined values of $\nu_{des} = 10^6$ mol/m^2/s and $\Delta E^{\ddagger}_{des} = 43$ kJ/mol used to create the dataset. The region of 95% confidence was calculated using the curvature of the χ^2 objective function around the global minimum (as explained in Sect. 4) and was drawn over the contour plot as a red ellipse. The ellipse contains a large area of the white region of the plot, spanning several orders of magnitude of ν_{des} and a large range of ϵ_{des}. All combinations of $\log(\nu_{des})$ and $\Delta E^{\ddagger}_{des}$ within this red error ellipse are capable of giving reasonable fits to the data, although not all combinations are physically meaningful (i.e. $\Delta E^{\ddagger}_{des} < 0$). Such a large uncertainty on these two parameters is due to the coupling of the pre-exponent and energy barrier in the Arrhenius equation (Eq. 9). The value of the desorption rate constant, k_{des}, stays constant when $\log(\nu_{des})$ is decreased at a rate proportional to the decrease in $\Delta E^{\ddagger}_{des}$. The same phenomenon can be observed when plotting χ^2 as a function of the other two pairs of $\log(\nu)$ and ϵ. This illustrates the inherent futility of trying to extract independent measures of $\log(\nu)$ and ΔE from kinetic data spanning a limited range of temperatures. Because all pairs of $\log(\nu)$ and ΔE are coupled in this way, one must turn to additional fundamental understanding of reaction rate constants in order to estimate either one of these two parameters. In this case, the pre-exponents can be estimated using transition state theory, thereby enabling meaningful estimation of $\Delta E^{\ddagger}_{ads}$, $\Delta E^{\ddagger}_{des}$, and ΔE_{ss} from the experimental dataset [43]. For the remainder of this work, we will limit parameter fitting to the quantities ($\Delta E^{\ddagger}_{ads}$, $\Delta E^{\ddagger}_{des}$, ΔE_{ss}) and fix the pre-exponential factors to their values estimated by transition state theory, i.e. ($\nu_{ads} = 10^2$ mol/m^2/s/Torr, $\nu_{des} = 10^6$ mol/m^2/s, and $\nu_{ss} = 10^0$) [43].

Using transition state theory to estimate the pre-exponent values involves its own inherent assumptions about the nature of the transition state. In the case of adsorption and desorption this typically involves assumptions about the mobility of the transition state. Given that the adsorption process for H_2 has no barrier and, therefore, that the desorption process has a transition state that is very late in the reaction coordinate, the transition state is likely to approximate H_2 weakly interacting with the surface. In other words, the transition state is mobile. In all such analyses, it necessary to be clear about the assumptions being made regarding the transition state. If the uncertainty in the transition state estimate of the pre-exponent is larger than that of the estimate based solely on the kinetic data (Fig. 4), then the use of transition state theory is unjustified.

One of the ubiquitous issues plaguing parameter estimation problems is the potential existence of multiple local minima in the objective function, χ^2, all predicting different sets of parameter values that yield comparably good fits to the data. Performing multiple fits using different initial seed parameters that span wide ranges (orders of magnitude) of parameter space can reveal multiple solutions or provide some confidence that a unique optimal solution has been found. Of course, this becomes impractical for problems with many degrees of freedom (i.e. too many fitting parameters). An interesting feature of the 2H′ model was discovered when allowing the search space for ΔE_{ss} to include negative values, i.e. implying exothermic surface-to-subsurface energetics. Figure 5 shows a grayscale contour plot of χ^2 versus ϵ_{ads} and ϵ_{ss} (with $\Delta E^{\ddagger}_{des} = 43$ kJ/mol, the value used for simulation of the dataset). The kinetic parameters used to create the dataset are indicated by the blue dot and an alternate minimum (optimal fit) is indicated by the green dot. Surprisingly, the solver found a new solution with $\chi^2 < 3\times10^{-9}$ at a value of $\Delta E_{ss} = -25$ kJ/mol, the negative of the value used to generate the dataset. At this solution, the adsorption energy barrier is $\Delta E^{\ddagger}_{ads} = 50$ kJ/mol, also substantially different from the value of $\Delta E^{\ddagger}_{ads} = 0$ kJ/mol used to generate the dataset. Note that these alternative values of ΔE_{ss} and $\Delta E^{\ddagger}_{ads}$ differ by exactly -50 and + 50 kJ/mol, respectively, from the values used to generate the dataset.

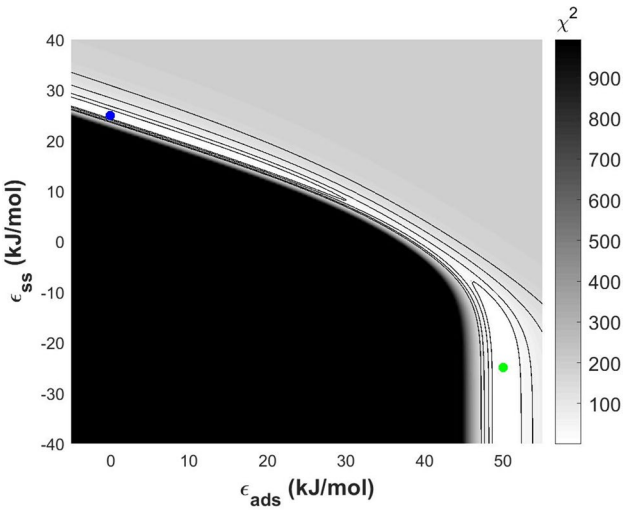

Fig. 5 Grayscale map and contour plot of χ^2 versus ϵ_{ads} and ϵ_{ss} calculated using the noiseless simulated dataset from Fig. 3. Note that χ^2 increases so quickly in the black region that all values of χ^2 in this region were assigned a maximum value of 1000. The expected minimum with $\Delta E_{ss} > 0$ is marked by the blue point and has $\chi^2 < 3\times10^{-9}$. An alternative solution with $\Delta E_{ss} < 0$ is marked by the green point and also has $\chi^2 < 3\times10^{-9}$

The value of $\Delta E^{\ddagger}_{des} = 43$ kJ/mol used to generate the dataset is also found for the second optimum fit.

To investigate the effect of the sign of ΔE_{ss} on the 2H′ model predictions, the total coverages of surface and subsurface hydrogen species were plotted as functions of temperature and total inlet hydrogen pressure, P_H^{tot}, in Fig. 6. The left-hand panels of Fig. 6 show the total coverages on the surface, θ, and in the subsurface, θ', predicted using the parameter values, $(\Delta E^{\ddagger}_{ads}, \Delta E^{\ddagger}_{des}, \Delta E_{ss}) = (0, 43, 25)$, used to create the dataset. The low value of $\Delta E^{\ddagger}_{ads} = 0$ kJ/mol results in high coverages on the surface, $\theta \approx 1$, while the positive value of $\Delta E_{ss} = 25$ kJ/mol, yields very low coverages in the subsurface, $\theta' \approx 0$. The right-hand panels of Fig. 6 show the coverages, θ and θ', predicted using the parameter values at the alternate minimum, $(\Delta E^{\ddagger}_{ads}, \Delta E^{\ddagger}_{des}, \Delta E_{ss}) = (50, 43, -25)$, marked by the green dot in Fig. 5. The high value of $\Delta E^{\ddagger}_{ads} = 50$ kJ/mol yields a very low coverage on the surface, $\theta \approx 0$, while the negative value of $\Delta E_{ss} = -25$ kJ/mol yields a high coverage in the subsurface, $\theta' \approx 1$. An apparent symmetry in the coverages at these two optimal sets of parameters leads to identical HD flow rates by swapping the values of θ and θ' in the 2H′ mechanism. In other words, the model is incapable of distinguishing between a saturated top surface with a depleted subsurface and a saturated subsurface with a depleted surface.

As a result of the indistinguishability of the two parameter sets identified by the fitting process, the values of ΔE_{ss} and $\Delta E^{\ddagger}_{ads}$ must be identified based on additional data. In this case, DFT calculations [29, 36] show that the exchange of hydrogen between the surface and the subsurface should be endothermic for Pd, consistent with the choice that $\Delta E_{ss} = 25$ kJ/mol. In addition, there are many experimental studies of the dissociative adsorption of H_2 on Pd surfaces [21, 28] indicating that the barrier to dissociative hydrogen adsorption on Pd is negligible, consistent with the choice of $\Delta E^{\ddagger}_{ads} = 0$ kJ/mol over the value of 50 kJ/mol suggested by the alternate solution.

3.3 Parameter Estimation from a Simulated Dataset with Noise

The dataset discussed in the previous section was simulated directly from the rate law (Eq. 7) with parameter values set at $(\Delta E^{\ddagger}_{ads}, \Delta E^{\ddagger}_{des}, \Delta E_{ss}) = (0, 43, 25)$ kJ/mol. The pre-exponential factors for the rate constants and equilibrium constant were set at values consistent with transition state theory, $(\nu_{ads}, \nu_{des}, \nu_{ss}) = (10^2$ mol/m^2/s/Torr, 10^6 mol/m^2/s, $10^0)$. To examine the performance of the solver on a dataset that more closely represents the experiment, random Gaussian noise with a standard deviation of 3% was introduced into the simulated data. The search space for all three energy parameters was bounded between 0 and 100 kJ/mol. As before, 1000 random initial seeds were generated across the search space and used to initialize minimization of χ^2. The result of the fitting is shown in Fig. 7, where the black dots are the simulated HD flow rates at the outlet, $F^{sim}_{HD}(T; P^{in}_{H_2}, P^{in}_{D_2})$, calculated using $(\Delta E^{\ddagger}_{ads}, \Delta E^{\ddagger}_{des}, \Delta E_{ss}) = (0,$

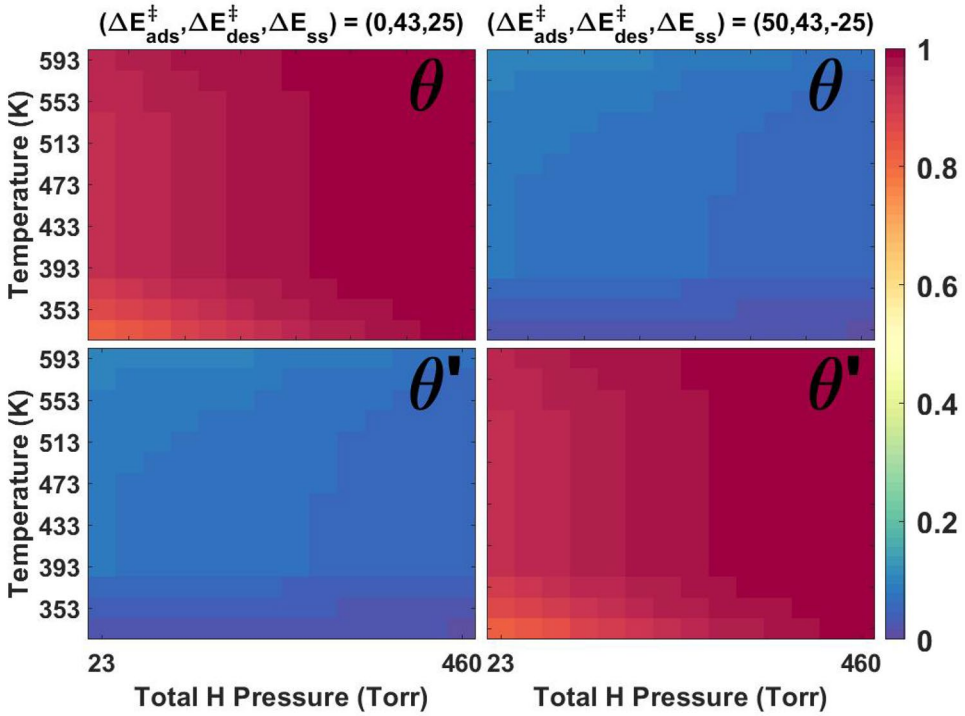

Fig. 6 The fractional coverage of H + D on the surface, θ, and H' + D' in the subsurface, θ', versus temperature and inlet $H_2 + D_2$ pressure, P_H^{tot}. The panels on the left show the coverages based on the parameters defined in the simulated dataset, with $\Delta E_{ss} = 25$ kJ/mol, $\Delta E^{\ddagger}_{ads} = 0$ kJ/mol, and $\Delta E^{\ddagger}_{des} = 43$ kJ/mol. The righthand panels show coverages on the surface and in the subsurface, θ and θ', for the symmetric solution found by the solver, where $\Delta E_{ss} = -25$ kJ/mol, $\Delta E^{\ddagger}_{ads} = 50$ kJ/mol, and $\Delta E^{\ddagger}_{des} = 43$ kJ/mol. This symmetry reveals that identical fits can be achieved by swapping the values of θ and θ' in the 2H' mechanism

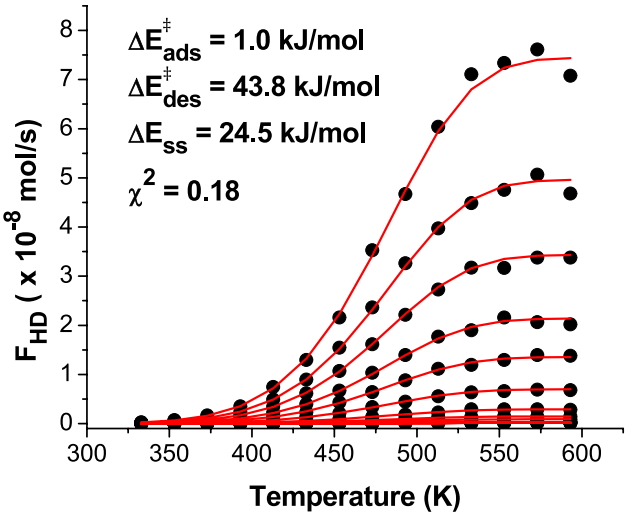

Fig. 7 Outlet HD flow rates versus temperature for 14 different feed flow conditions. The black dots represent the simulated data with the inclusion of 3% Gaussian noise. The red lines illustrate the result of fitting the 2H' model to the data. For the fitting, $\log(\nu_{ads})$, $\log(\nu_{des})$, and $\log(\nu_{ss})$ were fixed at their transition state theory values, and the search space for ΔE_{ss} was constrained to be ≥ 0 kJ/mol. The solver-predicted values for $\Delta E^{\ddagger}_{ads}$, $\Delta E^{\ddagger}_{des}$, and ΔE_{ss} are indicated on the graph and are close to the parameters used to generate the dataset. The value of χ^2 for the fit is 0.18

43, 25) kJ/mol with 3% Gaussian noise added. The solid red lines show the predicted values of $F^{solv}_{HD}(T;P^{in}_{H_2},P^{in}_{D_2})$ found using the estimated parameter values of $(\Delta E^{\ddagger}_{ads}, \Delta E^{\ddagger}_{des}, \Delta E_{ss})=(1.0, 43.8, 24.5)$ kJ/mol at the optimal solution. Introduction of Gaussian noise results in an increase in the minimum value of χ^2 to 0.18, however, the solver converged to the same parameter estimates for a wide range of initial guesses. As before, the solver only failed to find the optimal solution when the initial guess corresponded to either 0% or 100% ($H_2+D_2 \leftrightarrow 2HD$ equilibrium) conversion for all reaction conditions, (T, $P^{in}_{H_2}$, $P^{in}_{D_2}$). When the solver starts in these regions, the value of χ^2 is insensitive to changes in the kinetic parameters, ($\Delta E^{\ddagger}_{ads}$, $\Delta E^{\ddagger}_{des}$, ΔE_{ss}).

Figure 7 shows that even with noisy data the solver can yield close estimates of the kinetic parameters used to simulate the dataset. However, in most parameter estimation problems, the model parameters are unknown, and sometimes lack physical significance, making it more difficult to trust the output of the solver or constrain it to physically reasonable regions of parameter space. Relevant to this, it is important to note that extending the parameter space used for fitting the data with 3% noise into regions where $\Delta E_{ss} < 0$ results again in the identification of a second minimum, as shown in Fig. 5. The alternative solution occurs at ($\Delta E^{\ddagger}_{ads}$, $\Delta E^{\ddagger}_{des}$, ΔE_{ss})=(50, 43.8, -24.5) kJ/mol with $\chi^2 = 0.18$. This describes the scenario where the surface coverage is $\theta \approx 0$ and subsurface coverage is $\theta' \approx 1$ (as in Fig. 6), opposite to the coverages of the physically reasonable solution. The primary point to make is that the addition of 3% noise into the kinetic data only slightly degrades the ability of the 2H′ model to extract meaningful estimates of reaction parameters. The next issues to address are our ability to extract parameter estimates from the real kinetic data and how to quantify the confidence limits on those estimates.

4 Quantification of Confidence Limits on Estimated Kinetic Parameters

In order to quantify the confidence limits on the estimated kinetic parameters for the 2H′ mechanism, we assume a normal distribution around their most probable values, ($\Delta E^{\ddagger}_{ads}$, $\Delta E^{\ddagger}_{des}$, ΔE_{ss}), at the global minimum of $\chi^2(\epsilon_{ads}, \epsilon_{des}, \epsilon_{ss})$. Since the 2H′ mechanism used for the creation of the simulated datasets contains three parameters ($\Delta E^{\ddagger}_{ads}$, $\Delta E^{\ddagger}_{des}$, ΔE_{ss}), a 3D probability density function (PDF) defines the region in (ϵ_{ads}, ϵ_{des}, ϵ_{ss}) space within which the solution can be found with a given level of confidence (e.g. 68%, 95%, etc.). For a 3D parameter space, the probability, $\boldsymbol{P}$, of finding the solution within a certain 'distance', k, of the minimum of $\chi^2(\epsilon_{ads}, \epsilon_{des}, \epsilon_{ss})$ is defined by Eq. 12.

$$\boldsymbol{P}(k) = \mathrm{erf}\left(\frac{k}{\sqrt{2}}\right) - k\sqrt{\frac{2}{\pi}}\exp\left(-\frac{k^2}{2}\right) \tag{12}$$

The values of k for any desired confidence limit have been tabulated for PDFs of various dimensionality [44]. We are seeking the 95% confidence limit (i.e. the value of k at which $\boldsymbol{P}(k) = 0.95$) for the values of the three parameters, (ϵ_{ads}, ϵ_{des}, ϵ_{ss}), around their most probable values of $\Delta E^{\ddagger}_{ads}$, $\Delta E^{\ddagger}_{des}$, and ΔE_{ss} at the global minimum of $\chi^2(\epsilon_{ads}, \epsilon_{des}, \epsilon_{ss})$. For a 3D PDF, $\boldsymbol{P}(k) = 0.95$ when $k = 2.7955$ [44]. This value of $k = 2.7955$ determines the distance between the mean value of the kinetic parameters, ($\Delta E^{\ddagger}_{ads}$, $\Delta E^{\ddagger}_{des}$, ΔE_{ss}), and the locus of points that represent the 95% confidence limit in 3D. More precisely, k^2 serves as a scaling factor for a 3D hyper-ellipsoid centered on the global minimum of $\chi^2(\epsilon_{ads}, \epsilon_{des}, \epsilon_{ss})$ and whose orientation in parameter space is determined by the covariance of the three fitting parameters, as derived from the fitting process.

The orientation of the 3D hyper-ellipsoid comes from the covariance matrix ($\bar{\bar{C}}$), which defines the variances of all three fitting parameters and the covariances between each pair of parameters (Eq. 13). The covariance matrix is found by inverting the Hessian ($\bar{\bar{\mathcal{H}}}$) matrix, which is calculated each time the solver converges. The Hessian matrix contains all of the second derivatives and cross derivatives of χ^2 with respect to ϵ_{ads}, ϵ_{des}, and ϵ_{ss}, evaluated at ($\Delta E^{\ddagger}_{ads}$, $\Delta E^{\ddagger}_{des}$, ΔE_{ss}).

In physical terms, $\bar{\bar{\mathcal{H}}}$, characterizes the curvature of χ^2 around its global minimum.

$$\bar{\bar{C}} = \bar{\bar{\mathcal{H}}}^{-1} = \begin{bmatrix} \sigma^2_{\epsilon_{ads}} & \rho_{\epsilon_{ads}\epsilon_{des}}\sigma_{\epsilon_{ads}}\sigma_{\epsilon_{des}} & \rho_{\epsilon_{ads}\epsilon_{ss}}\sigma_{\epsilon_{ads}}\sigma_{\epsilon_{ss}} \\ \rho_{\epsilon_{ads}\epsilon_{des}}\sigma_{\epsilon_{ads}}\sigma_{\epsilon_{des}} & \sigma^2_{\epsilon_{des}} & \rho_{\epsilon_{des}\epsilon_{ss}}\sigma_{\epsilon_{des}}\sigma_{\epsilon_{ss}} \\ \rho_{\epsilon_{ads}\epsilon_{ss}}\sigma_{\epsilon_{ads}}\sigma_{\epsilon_{ss}} & \rho_{\epsilon_{des}\epsilon_{ss}}\sigma_{\epsilon_{des}}\sigma_{\epsilon_{ss}} & \sigma^2_{\epsilon_{ss}} \end{bmatrix} \tag{13}$$

In Eq. 13, σ represents the standard deviation for each parameter and ρ represents the correlation coefficient for each pair of parameters. In order to encompass the entire 95% confidence region, the distance from the center of the hyper-ellipsoid at $(\Delta E^{\ddagger}_{ads}, \Delta E^{\ddagger}_{des}, \Delta E_{ss})$ to its surface must equal the Mahalanobis distance, $k^2 = 7.8148$ [44]. While k^2 is a constant, the absolute distance between the center point and the surface of the hyper-ellipsoid changes based upon the variance and covariance of the parameters at the global minimum. Combining all of these features, the equation for the 3D hyper-ellipsoid in the Cartesian coordinate system $(\epsilon_{ads}, \epsilon_{des}, \epsilon_{ss})$ is given by Eq. 14.

$$\begin{aligned} k^2 = & \frac{\left(\epsilon_{ads} - \Delta E^{\ddagger}_{ads}\right)^2}{\sigma^2_{\epsilon_{ads}}} + \frac{\left(\epsilon_{des} - \Delta E^{\ddagger}_{des}\right)^2}{\sigma^2_{\epsilon_{des}}} + \frac{\left(\epsilon_{ss} - \Delta E_{ss}\right)^2}{\sigma^2_{\epsilon_{ss}}} \\ & + 2\frac{(\epsilon_{ads} - \Delta E^{\ddagger}_{ads})(\epsilon_{des} - \Delta E^{\ddagger}_{des})}{\rho_{\epsilon_{ads}\epsilon_{des}}\sigma_{\epsilon_{ads}}\sigma_{\epsilon_{des}}} \\ & + 2\frac{(\epsilon_{ads} - \Delta E^{\ddagger}_{ads})(\epsilon_{ss} - \Delta E_{ss})}{\rho_{\epsilon_{ads}\epsilon_{ss}}\sigma_{\epsilon_{ads}}\sigma_{\epsilon_{ss}}} \\ & + 2\frac{(\epsilon_{des} - \Delta E^{\ddagger}_{des})(\epsilon_{ss} - \Delta E_{ss})}{\rho_{\epsilon_{des}\epsilon_{ss}}\sigma_{\epsilon_{des}}\sigma_{\epsilon_{ss}}} \end{aligned} \tag{14}$$

Dividing both sides of Eq. 14 by k^2 results in the standard ellipsoid equation and causes k^2 to act as a scaling factor for each term in the covariance matrix. Equation 14 can be condensed into linear algebra notation, as shown in Eq. 15.

$$1 = \left(\begin{bmatrix} \epsilon_{ads} \\ \epsilon_{des} \\ \epsilon_{ss} \end{bmatrix} - \begin{bmatrix} \Delta E^{\ddagger}_{ads} \\ \Delta E^{\ddagger}_{des} \\ \Delta E_{ss} \end{bmatrix}\right)^T \left(k^2 \cdot \bar{\bar{C}}\right)^{-1} \left(\begin{bmatrix} \epsilon_{ads} \\ \epsilon_{des} \\ \epsilon_{ss} \end{bmatrix} - \begin{bmatrix} \Delta E^{\ddagger}_{ads} \\ \Delta E^{\ddagger}_{des} \\ \Delta E_{ss} \end{bmatrix}\right) \tag{15}$$

Plotting Eq. 15 in $(\epsilon_{ads}, \epsilon_{des}, \epsilon_{ss})$ parameter space allows visualization of the 3D hyper-ellipsoid centered on the global minimum of χ^2 at $(\Delta E^{\ddagger}_{ads}, \Delta E^{\ddagger}_{des}, \Delta E_{ss})$. For the noiseless simulated dataset, the resulting ellipsoid is a wide, thin shape, as shown in Fig. 8. The true values of $\Delta E^{\ddagger}_{ads}$, $\Delta E^{\ddagger}_{des}$, and ΔE_{ss} lie within this ellipsoidal region with up to 95% confidence. However, this 3D region of parameter space is difficult to visualize and quantify in a straightforward way.

In parameter estimation problems with more than three degrees of freedom, it is impossible to visualize these hyper-ellipsoidal regions of parameter space. Furthermore, when parameters are coupled, it is meaningless to try to represent the uncertainty of a given parameter using a single value. If the covariance matrix, $\bar{\bar{C}}$, was diagonal, then the three major axes of the 3D hyper-ellipsoid would be parallel to the ϵ_{ads}, ϵ_{des}, and ϵ_{ss} axes and the PDF would be described by a product of three normal distribution functions, one for each degree of freedom. These three normal distribution functions would also define the variances for each degree of freedom, $(\sigma^2_{\epsilon_{ads}}, \sigma^2_{\epsilon_{des}}, \sigma^2_{\epsilon_{ss}})$, and the hyper-ellipsoid would be defined by Eq. 14 with just the first three terms of the right-hand side. Under these conditions, the confidence regions for each of the three degrees of freedom can be meaningfully represented by a unique value. However, as illustrated in Fig. 8, this is not the case for the 2H′ mechanism. Nor is it true for the 1H′ or LH mechanisms. When parameters are coupled, the confidence intervals must be represented by continuous regions spanning multiple degrees of freedom in parameter space.

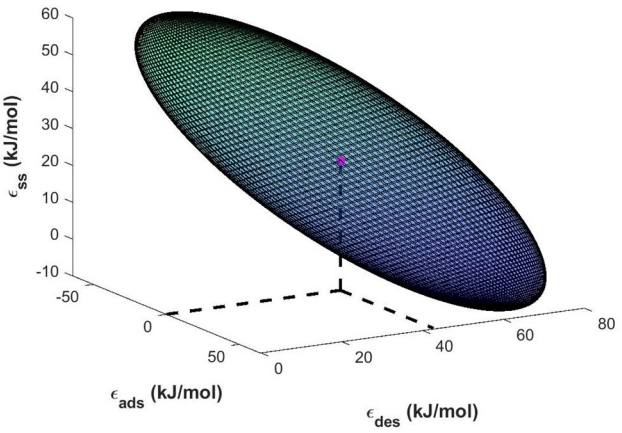

Fig. 8 The 3D hyper-ellipsoid for the noiseless simulated dataset encloses the 95% confidence region around the global minimum of χ^2, marked by the pink dot at $(\Delta E^{\ddagger}_{ads}, \Delta E^{\ddagger}_{des}, \Delta E_{ss}) = (0, 43, 25)$ kJ/mol. The translucent hyper-ellipsoid is constructed using the Hessian matrix returned by the solver, quantifying the curvature of χ^2 with respect to all three parameters. The black dashed lines serve as aids for visualizing the 3D hyper-ellipsoid with respect to the axes

One method for portraying the confidence regions contained within the hyper-ellipsoid is to project them onto each of the 2D planes spanned by the pairs of natural variables for the problem, e.g. $(\epsilon_{ads}, \epsilon_{des})$. An error ellipse is a 2D section or projection of the n-dimensional hyper-ellipsoid centered on the estimated values of the fitting parameters: $\Delta E^{\ddagger}_{ads}$, $\Delta E^{\ddagger}_{des}$, and ΔE_{ss}. For example, one could take the ellipsoid illustrated in Fig. 8 and project it onto the $(\epsilon_{ads}, \epsilon_{des})$ plane as a 2D ellipse centered on the most probable values $(\Delta E^{\ddagger}_{ads}, \Delta E^{\ddagger}_{des})$. This would define the region of 95% confidence for finding $\Delta E^{\ddagger}_{ads}$ and $\Delta E^{\ddagger}_{des}$, independent of the value of ΔE_{ss}.

This overestimates the confidence region because it includes points at which finding the values $(\Delta E^{\ddagger}_{ads}, \Delta E^{\ddagger}_{des}, \Delta E_{ss})$ is highly improbable. An alternative representation of the confidence region is to take the 2D cross section of the 3D hyper-ellipsoid in a plane parallel to $(\epsilon_{ads}, \epsilon_{des})$ at a value of $\epsilon_{ss} = \Delta E_{ss}$. This represents the region of 95% confidence for finding $\Delta E^{\ddagger}_{ads}$ and $\Delta E^{\ddagger}_{des}$ when ΔE_{ss} takes its most probable value. In the figures below, we have used these 2D cross sections through the hyper-ellipsoid evaluated at the most probable value of the third degree of freedom.

Figure 9 presents a graphical visualization of the 2D cross sections through the 3D hyper-ellipsoids for: the noiseless simulated data (left column), the simulated data with 3% noise (middle column), and the experimental data on Pd (right column). These are all plotted in 2D parameter space and are superimposed on contour plots of $\chi^2(\epsilon_{ads}, \epsilon_{des}, \epsilon_{ss})$. Each contour plot was constructed by holding one of the energy parameters constant at its most probable value ($\Delta E^{\ddagger}_{ads}$, $\Delta E^{\ddagger}_{des}$, or ΔE_{ss}) and allowing the other two parameters to vary over a range of values while explicitly calculating χ^2 at each point. The blue dot marked on each graph shows the global minimum found by the solver at $(\Delta E^{\ddagger}_{ads}, \Delta E^{\ddagger}_{des}, \Delta E_{ss})$. The solid red ellipses drawn over the contour plots for the three datasets represent the intersections of their associated hyper-ellipsoids with the three 2D planes evaluated at the most probable value of the third parameter. The loci of points on these ellipses are solutions to Eqs. 14 or 15 defining the 3D hyper-ellipsoid. The hyper-ellipsoids constructed for each of the three datasets are similar in orientation and size, as revealed by the similarity of the solid red ellipses along each row in Fig. 9. It is worth noting that the error ellipses for the noiseless simulated data (Figs. 9a, d, and g) represent the theoretical "best" (i.e. smallest) confidence limits from fitting the 2H′ model to the dataset.

In reality, the χ^2 function is not perfectly parabolic as implied by the Gaussian assumption. This is seen clearly in the top and bottom rows of Fig. 9 where the solid red ellipses span a range of contour levels and χ^2 starts to deviate significantly from its value at the global minimum. In the quadratic approximation, the value of $\chi^2 \cong \chi^2_{(2)}$ where $\chi^2_{(2)}$ at a constant value of ΔE_{ss} is given by the following expression

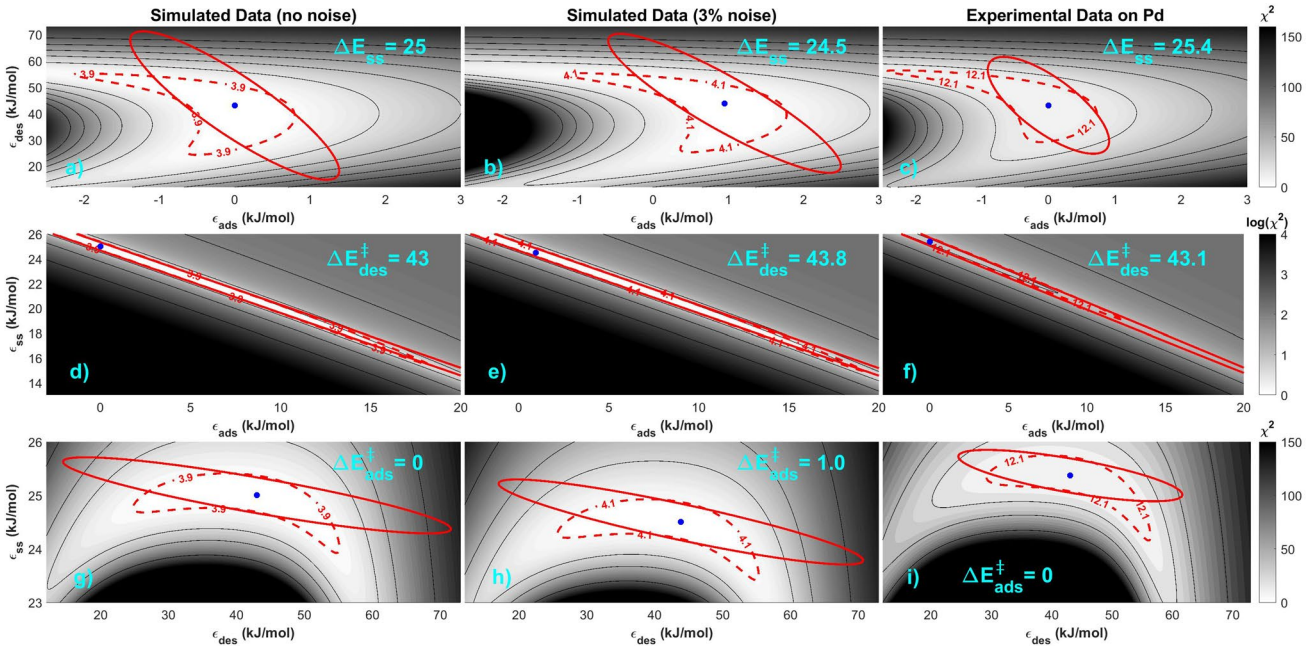

Fig. 9 Grayscale contour plots of $\chi^2(\epsilon_{ads}, \epsilon_{des}, \epsilon_{ss})$ around the global minimum (marked in blue) for: **a**, **d**, **g** the noiseless simulated data for the 2H' mechanism, **b**, **e**, **h** the simulated data with 3% noise, and **c**, **f**, **i** the experimental data on Pd. Each χ^2 contour map was evaluated as a function of two parameters while holding the third at its most probable value. The solid red error ellipses represent the intersection of the 3D hyper-ellipsoid with the three planes in parameter space. The region bounded by each error ellipse represents the region of 95% confidence assuming that χ^2 is perfectly quadratic around its minimum. Evaluation of χ^2 at any point on the red ellipses using the Taylor expansion (Eq. 16) yields: ${}_{95}\chi^2_{(2)} = 3.9$ for the simulated 2H' data with no noise, ${}_{95}\chi^2_{(2)} = 4.1$ for the simulated data with 3% noise, and ${}_{95}\chi^2_{(2)} = 12.1$ for the experimental data on Pd. Contour levels at these three values are marked with dotted red lines on each plot and are used to represent the 95% confidence regions

$$\chi^2_{(2)}\left(\Delta E^{\ddagger}_{ads}+\delta_{ads},\Delta E^{\ddagger}_{des}+\delta_{des},\Delta E_{ss}\right)\approx\chi^2_{min}+\frac{1}{2}\frac{d^2\chi^2}{d\epsilon^2_{ads}}\bigg|_{\Delta E^{\ddagger}_{ads},\Delta E^{\ddagger}_{des},\Delta E_{ss}}\cdot\delta_{ads}{}^2+\frac{1}{2}\frac{d^2\chi^2}{d\epsilon^2_{des}}\bigg|_{\Delta E^{\ddagger}_{ads},\Delta E^{\ddagger}_{des},\Delta E_{ss}}\cdot\delta_{des}{}^2+\frac{d^2\chi^2}{d\epsilon_{ads}d\epsilon_{des}}\bigg|_{\Delta E^{\ddagger}_{ads},\Delta E^{\ddagger}_{des},\Delta E_{ss}}\cdot\delta_{ads}\delta_{des}\tag{16}$$

in which $\chi^2_{min}=\chi^2(\Delta E^{\ddagger}_{ads},\Delta E^{\ddagger}_{des},\Delta E_{ss})$. The second derivatives of χ^2 with respect to ϵ_{ads} and ϵ_{des} are evaluated at the global minimum and come directly from the Hessian matrix returned by the solver. The value of $\chi^2_{(2)}$ is constant on the locus of points forming the ellipsoid; i.e. on the solid red ellipses indicating the intersection of the 3D hyper-ellipsoid with the 2D planes through (ϵ_{ads}, ϵ_{des}, ϵ_{ss}) space shown in Fig. 9. In this case, the value of $\chi^2_{(2)}$ on the ellipse can be denoted ${}_{95}\chi^2_{(2)}$, the value that determines the 95% confidence limit. Since much of the area contained within the solid red ellipses includes parameters that yield relatively poor fits to the data, we also highlight as a dashed red curve the contour level along which $\chi^2={}_{95}\chi^2_{(2)}$. The dashed red contour provides a better estimate of the 95% confidence region than the solid red ellipse.

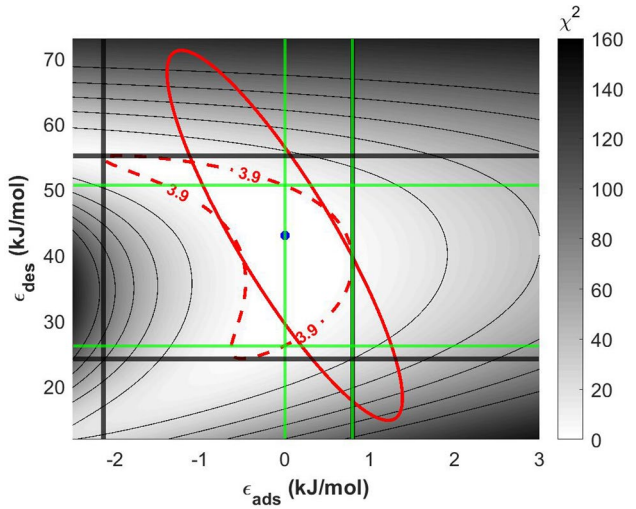

Fig. 10 Grayscale contour plot of χ^2 versus ϵ_{ads} and ϵ_{des} at ΔE_{ss} = 25 kJ/mol for the noiseless data simulated using the 2H' mechanism. The global minimum is marked by the blue dot and the solid red error ellipse indicates the region of 95% confidence predicted from $\chi^2_{(2)}$, the quadratic approximation to χ^2. Calculation of $\chi^2_{(2)}$ at any point on the red ellipse using the Taylor expansion (Eq. 16) yields ${}_{95}\chi^2_{(2)}$ = 3.9. The corresponding contour of χ^2 at the value of 3.9 is marked by the dashed red curve. The solid black lines framing the contour level at χ^2 = 3.9 provide conservative estimates of the 95% confidence limits on $\Delta E^{\ddagger}_{ads}$ and $\Delta E^{\ddagger}_{des}$. A subset of the region contained within the black lines is bounded by green lines which account for the constraint that only solutions with $\Delta E^{\ddagger}_{ads}>0$ are physically meaningful. Thus, the area framed by the green rectangle represents the estimated 95% confidence region for $\Delta E^{\ddagger}_{ads}$ and $\Delta E^{\ddagger}_{des}$ when ΔE_{ss} is fixed at 25 kJ/mol

Figure 10 shows the same contour plot as in Fig. 9a. The quadratic Taylor expansion at any point on the solid red ellipse has a constant value of ${}_{95}\chi^2_{(2)}=3.9$. As a better estimate of the 95% confidence interval, we have mapped with a dashed red curve the region of parameter space bounded by the locus of points on the $\chi^2=3.9$ contour. This region serves as a better representation than the ellipse of the parameter space within which combinations of (ϵ_{ads}, ϵ_{des}, ΔE_{ss}) yield statistically indistinguishable fits of the 2H′ mechanism to the data.

Figure 10 also includes four solid black lines drawn at the maximum and minimum values of ϵ_{ads} and ϵ_{des} at which $\chi^2=3.9$. However, not all of the parameter space contained within the black rectangle is realistic because it includes values of $\Delta E^{\ddagger}_{ads}<0$ that are nonphysical. Therefore, a subset of this region is framed by the green lines which contain the 95% confidence limit around $\Delta E^{\ddagger}_{ads}$ and $\Delta E^{\ddagger}_{des}$, constrained to include only physically meaningful values of ϵ_{ads} and ϵ_{des}. These limits serve as conservative estimates for the 95% confidence limits on $\Delta E^{\ddagger}_{ads}$ and $\Delta E^{\ddagger}_{des}$. The contour level at $\chi^2=3.9$ is only achievable for values of ϵ_{ads} in the range 0 to 0.8 kJ/mol. Thus, the 95% confidence limit around $\Delta E^{\ddagger}_{ads}$ = 0 kJ/mol spans the range [0, 0.8] kJ/mol. Similarly, Fig. 10 reveals that the 95% confidence limit around $\Delta E^{\ddagger}_{des}$ = 43 kJ/mole spans the range [26, 51] kJ/mol.

All of the solid red error ellipses in Fig. 9 have been mapped onto their corresponding contours at $\chi^2={}_{95}\chi^2_{(2)}$ using the dashed red curves. The Taylor expansion gives the same value of ${}_{95}\chi^2_{(2)}$ on all three 2D representations of the 3D hyper-ellipsoid because they all represent cross sections through the same ellipsoid. The values of ${}_{95}\chi^2_{(2)}$ get progressively higher for the simulated data with 3% noise (${}_{95}\chi^2_{(2)}=4.1$) and for the Pd experimental data (${}_{95}\chi^2_{(2)}=12.1$). Finding the extrema of the χ^2 contour level at 95% confidence gives a straightforward method for using χ^2 to estimate the uncertainties on all kinetic parameters. Note that this approach for estimating confidence limits on individual parameters is conservative. It implies a confidence region defined by a rectangular area (framed by the green lines in Fig. 10) that bounds the 95% confidence region (dashed red contour). This rectangular area contains regions that represent combinations of ϵ_{ads} and ϵ_{des} that lie outside the dashed contour defining the 95% confidence region. Note also, that this analysis takes advantage of the fact that we have evaluated $\chi^2(\epsilon_{ads},\epsilon_{des},\epsilon_{ss})$ across the full 3D parameter space. In general, this is not practical and one must rely only on the value of χ^2 at its minimum, χ^2_{min}, and on the Hessian to define the hyper-ellipsoid shown in Fig. 8. One would then estimate the intervals of individual parameters based on the extrema of the solid red

ellipses formed by the intersection of 2D planes with the hyper-ellipsoid under the assumption that χ^2 is quadratic in all degrees of freedom.

Analysis of the simulated datasets with and without the inclusion of Gaussian noise reveals the care with which parameter estimation must be performed. The coupling of kinetic parameters creates relatively large regions of parameter space across which the quality of the fit of the 2H′ mechanistic model is indistinguishable from the best fit to the data. This is particularly apparent in Figs. 5 and 9d, e, and f which plot $\chi^2\left(\epsilon_{ads}, \Delta E^{\ddagger}_{des}, \epsilon_{ss}\right)$, revealing a long narrow trough in χ^2 leading from a minimum at a low value of $\Delta E^{\ddagger}_{ads}$ and a positive ΔE_{ss} to a symmetric solution at a high value of $\Delta E^{\ddagger}_{ads}$ and a negative value of ΔE_{ss}. The presence of the alternate solutions reveals a challenge for fitting the 2H′ mechanism, namely the model's inability to differentiate between solutions having high surface coverage of H with low subsurface coverage of H′ and solutions having low surface coverage of H with high subsurface coverage of H′ (Fig. 6). In this case, the challenge has to be resolved by invoking the constraint that $\Delta E^{\ddagger}_{ads}$ should be low and $\Delta E_{ss} > 0$ to be consistent with prior observations [28–30, 36, 39].

To summarize, the methodology for the quantification of parameter confidence intervals takes advantage of the Hessian matrix returned by the solver at the global minimum of $\chi^2(\epsilon_{ads}, \epsilon_{des}, \epsilon_{ss})$. Using the curvature of χ^2 around the most probable parameter values, $(\Delta E^{\ddagger}_{ads}, \Delta E^{\ddagger}_{des}, \Delta E_{ss})$, allows construction of a hyper-ellipsoid bounding the region in which the values of $(\Delta E^{\ddagger}_{ads}, \Delta E^{\ddagger}_{des}, \Delta E_{ss})$ can be found with any desired level of confidence. This hyper-ellipsoid can be visualized on 2D planes spanning any pair of parameters by intersecting the hyper-ellipsoid at the most probable estimated value of the remaining parameter. Since χ^2 exhibits non-quadratic behavior over parameter space, we have identified the contours of $\chi^2 = {}_{95}\chi^2_{(2)}$, where ${}_{95}\chi^2_{(2)}$ is the quadratic approximation to χ^2 evaluated on the surface of the 95% confidence ellipsoid. This region of parameter space better estimates the 95% confidence region than the error ellipses. Using this method, we now turn to fitting the experimental data for H_2–D_2 exchange over the Pd catalyst using the three mechanistic adsorption/reaction models: LH, 1H′, and 2H′. It is important to note that for the 2H′ and 1H′ mechanisms, the 95% confidence limits for each parameter are given in two separate 2D plots, each representing a different cross section through the 3D hyper-ellipsoid. For example, the uncertainty range on $\Delta E^{\ddagger}_{ads}$ is given by $\chi^2\left(\epsilon_{ads}, \epsilon_{des}, \Delta E_{ss}\right)$ and by $\chi^2(\epsilon_{ads}, \Delta E^{\ddagger}_{des}, \epsilon_{ss})$. When these 95% confidence limits differ, we combine the ranges to encompass the parameter values from both plots so that the estimate of the 95% confidence region is more conservative.

5 Fitting H_2–D_2 Exchange Data for the Pd Catalyst

Three different mechanistic models, LH, 1H′, and 2H′, were fit to the experimental dataset for the H_2–D_2 exchange activity of the Pd catalyst. Derivations of the rate laws for each model have been provided elsewhere [33]. In brief, the subsurface mechanisms modify the LH model by including either one or two subsurface H′ atoms that influence the adsorption and desorption kinetics on the adjacent surface sites (Fig. 2). The expressions for the molar flow rate of product HD, $F^{out}_{HD}(T; P^{in}_{H_2}, P^{in}_{D_2})$, for the LH and 1H′ models are given in Eqs. 17 and 18, respectively.

$$F^{LH}_{HD} = \frac{2k_{des}\theta_H\theta_D F^{tot}}{k_{ads}(1-\theta)^2 P^{tot}}\left[1 - \exp\left(-\frac{Ak_{ads}(1-\theta)^2 P^{tot}}{F^{tot}}\right)\right] \tag{17}$$

$$F^{1H'}_{HD} = \frac{2k_{des}\theta_H\theta_D F^{tot}}{k_{ads}(1-\theta)^2 P^{tot}}\left[1 - \exp\left(-\frac{Ak_{ads}(1-\theta)^2\theta' P^{tot}}{F^{tot}}\right)\right] \tag{18}$$

The expressions for the coverages of H and D atoms on the surface and in the subsurface, θ_H, θ_D, θ, and θ', are given by Eqs. 2 – 5. The expression for F^{out}_{HD} given by each model was used to define χ^2 (Eq. 11) when fitting that model to the data. As for the datasets just presented for the 2H′ model, the

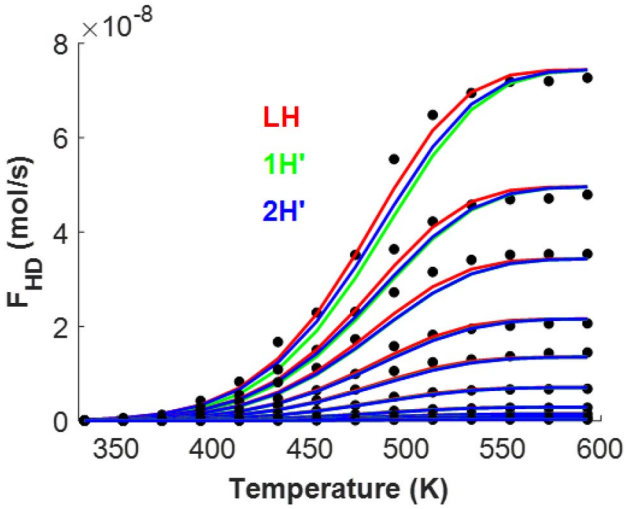

Fig. 11 Plot of HD outlet flow rate as a function of temperature for H_2–D_2 exchange on Pd. The black symbols are the experimentally measured HD flow rates exiting the microreactor array for 14 different inlet combinations of $P^{in}_{H_2}$ and $P^{in}_{D_2}$ and measured at 14 temperatures. The solid lines represent the solutions calculated using kinetic parameters found by the solver for the three different mechanisms: red = LH ($\Delta E^{\ddagger}_{ads}$ = 51.1, $\Delta E^{\ddagger}_{des}$ = 0 kJ/mol, χ^2_{min} = 6.4), green = 1H' ($\Delta E^{\ddagger}_{ads}$ = 0, $\Delta E^{\ddagger}_{des}$ = 20, ΔE_{ss} = 46 kJ/mol, χ^2_{min} = 10.4), and blue = 2H' ($\Delta E^{\ddagger}_{ads}$ = 0, $\Delta E^{\ddagger}_{des}$ = 43, ΔE_{ss} = 25 kJ/mol, χ^2_{min} = 8.2)

pre-exponents predicted by transition state theory were used when fitting each model to the kinetic data.

The experimental data, $F_{HD}^{out}\left(T;P_{H_2}^{in},P_{D_2}^{in}\right)$, for H_2–D_2 exchange over the Pd catalyst are compared in Fig. 11 to the predictions of the three reaction mechanisms determined using the optimal values of the kinetic parameters, ($\Delta E_{ads}^{\ddagger}$, $\Delta E_{des}^{\ddagger}$, ΔE_{ss}), found for each mechanism. In Fig. 11, the red curves represent the best fit using the LH mechanism, the green curves represent the best fit using the 1H′ mechanism, and the blue curves represent the best fit using the 2H′ mechanism. All three models produce nearly equivalent fits to the experimental data across all inlet flow conditions and temperatures, however, the best fits are achieved by different optimal values of the kinetic parameters.

Before comparing the three models, the 95% confidence limits on the estimated kinetic parameters are visualized using contour plots of χ^2, as was done for the 2H′ mechanism. Figure 12 shows the contour plot of $\chi_{LH}^2(\epsilon_{ads},\epsilon_{des})$ for the LH model fit to the H_2–D_2 exchange kinetics on the Pd catalyst. The global minimum found by the solver at ($\Delta E_{ads}^{\ddagger}$, $\Delta E_{des}^{\ddagger}$) = (51.1, 0) kJ/mol is marked by the blue dot and has a value of $\chi_{min}^2 = \chi^2(\Delta E_{ads}^{\ddagger},\Delta E_{des}^{\ddagger}) = 6.4$. The values of the kinetic parameters at this global minimum have been used with the LH model to simulate the values of $F_{HD}^{LH}(T;P_{H_2}^{in},P_{D_2}^{in})$ shown by the red curves in Fig. 11. The error ellipse defining the 95% confidence limit in the quadratic approximation for χ^2 about its minimum is not shown in Fig. 12 because it extends far outside the axis bounds due to the large variance

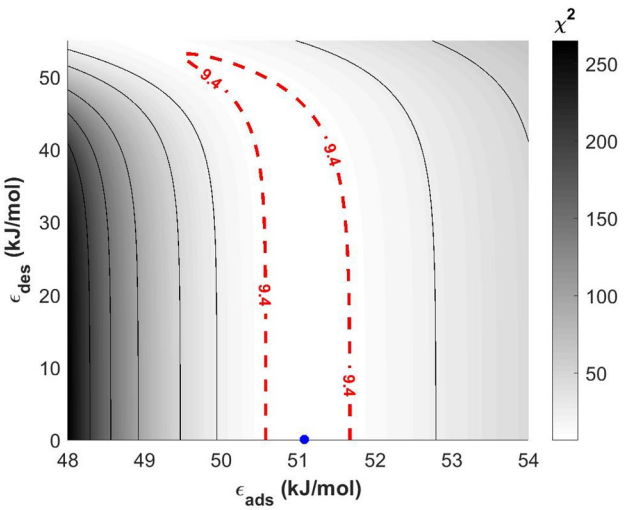

Fig. 12 Grayscale contour plot of $\chi_{LH}^2(\epsilon_{ads},\epsilon_{des})$ given by the LH model for H_2–D_2 exchange on Pd. The minimum point with χ_{min}^2 = 6.4 is marked in blue at $\Delta E_{ads}^{\ddagger}$ = 51.1 kJ/mol and $\Delta E_{des}^{\ddagger}$ = 0. The 95% confidence region is outlined by the dashed red contour at ${}_{95}\chi_{(2)}^2$ = 9.4. A trough runs parallel to the ϵ_{des} axis from $\epsilon_{des} = \Delta E_{des}^{\ddagger} = 0$ to ~ 50 kJ/mol, suggesting that the Pd surface is operating in a low coverage, adsorption limited regime

of ϵ_{des}. The value of $\chi_{(2)}^2$ for the LH mechanism on the 95% confidence ellipsoid is ${}_{95}\chi_{(2)}^2 = 9.4$. The contour on which $\chi_{LH}^2 = 9.4$ is shown as the dashed red curve in Fig. 12. χ_{LH}^2 = 9.4 has a trough at $\epsilon_{ads} = \Delta E_{ads}^{\ddagger} = 51.1$ kJ/mol running parallel to the ϵ_{des} axis from the minimum in χ_{LH}^2 at $\Delta E_{des}^{\ddagger}$ = 0 kJ/mol to $\epsilon_{des} \approx 50$ kJ/mol. Along this trough, the value of χ_{LH}^2 is independent of ϵ_{des} and all points along the trough yield good fits to the data. The values of ϵ_{ads} and ϵ_{des} along this trough suggest that the Pd catalyst is operating in a regime that is rate limited by adsorption. Therefore, the fitting cannot produce a meaningful estimate of $\Delta E_{des}^{\ddagger}$ for the LH model. The estimate for $\Delta E_{ads}^{\ddagger}$, however, possesses a high level of confidence around the optimal value of $\Delta E_{ads}^{\ddagger}$ = 51.1 kJ/mol, with the 95% confidence limit ranging from 50.6 to 51.7 kJ/mol. The combination of a high barrier to adsorption and a low barrier to desorption suggests that the Pd catalyst is operating in the low coverage limit. That, and the very high barrier to adsorption, $\Delta E_{ads}^{\ddagger}$ = 51.1 kJ/mol, suggests that this result is not physically realistic, i.e. although the LH model is capable of fitting our experimental data, it is not a good model for the H_2–D_2 exchange process.

The 1H′ and 2H′ mechanisms for H_2–D_2 exchange each have three degrees of freedom so their 95% confidence ellipsoids must be illustrated by three 2D plots of χ^2 versus two degrees of freedom and evaluated at the most probable value of the third. Figure 13 shows the contour plots of $\chi_{1H'}^2$ versus each pair of kinetic parameters for the fit of the 1H′ mechanism to the experimental data. Similarly, Fig. 14 shows the equivalent $\chi_{2H'}^2$ plots for the fit of the 2H′ mechanism to the data. In all cases, the global minimum is marked by a blue dot. The parameter values at the minimum were used to construct the solid green and blue curves in Fig. 11 showing $F_{HD}^{out}(T;P_{H_2},P_{D_2})$ predicted by the 1H′ and 2H′ models, respectively. The red ellipses in Figs. 13 and 14 bound the 95% confidence regions estimated by assuming a quadratic form for $\chi_{1H'}^2$ and $\chi_{2H'}^2$ about their minima, analogous to the red ellipses in Figs. 9 and 10. Using the quadratic Taylor expansion around the global minima yields estimates of the values of χ^2 on the 95% confidence ellipsoids: ${}_{95}\chi_{(2)}^2 = 14.3$ for the 1H′ model and ${}_{95}\chi_{(2)}^2 = 12.1$ for the 2H′ model. The contours of $\chi_{1H'}^2 = 14.3$ and $\chi_{2H'}^2 = 12.1$ are indicated by the dashed red curves in Figs. 13 and 14, respectively. Finally, the solid black lines on each plot are drawn at the extrema of the contours bounding the 95% confidence regions. It is important to note that these bounds on the values of the individual parameters are a conservative estimate of the real shape of the 95% confidence region. They are conservative in the sense that the rectangles bounding the 95% confidence regions contains areas that are not actually within the perimeter of the 95% confidence region. A summary of the fitting results and the 95% confidence limits for the kinetic

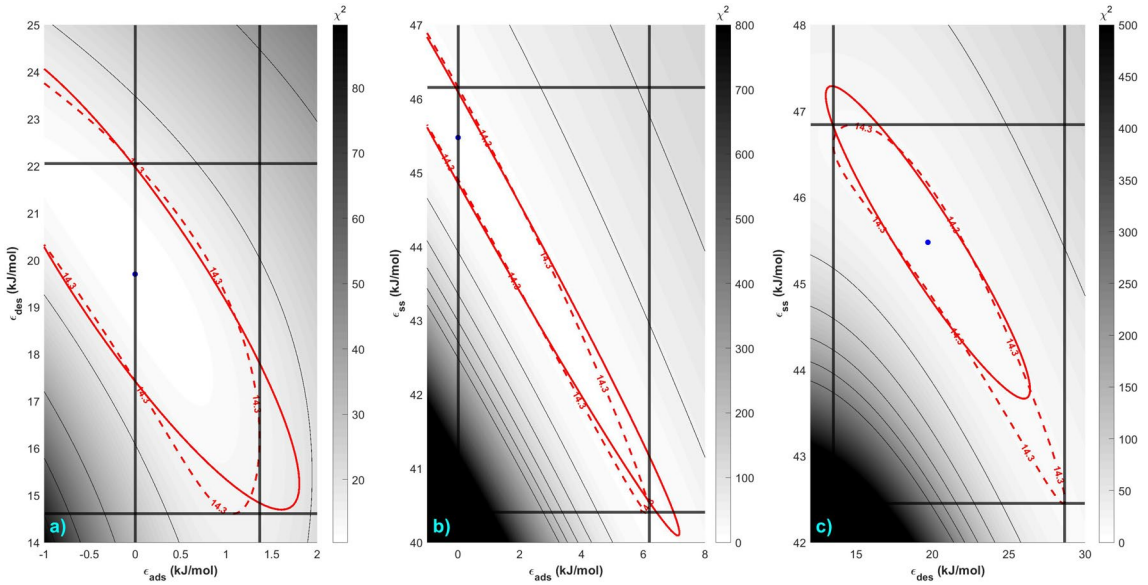

Fig. 13 Grayscale contour plots of **a** $\chi^2_{1H'}(\epsilon_{ads}, \epsilon_{des})$ with ΔE_{ss} = 46 kJ/mol, **b** $\chi^2_{1H'}(\epsilon_{ads}, \epsilon_{ss})$ with $\Delta E^{\ddagger}_{des}$ = 20 kJ/mol, and c) $\chi^2_{1H'}(\epsilon_{des}, \epsilon_{ss})$ with $\Delta E^{\ddagger}_{ads}$ = 0 given by the 1H' model for H_2–D_2 exchange on Pd. In all three plots, the blue dot marks the global minimum at $\Delta E^{\ddagger}_{ads}$ = 0, $\Delta E^{\ddagger}_{des}$ = 20 kJ/mol, and ΔE_{ss} = 46 kJ/mol with χ^2_{min} = 10.4. The red error ellipses represent the 95% confidence limit assuming a quadratic form for $\chi^2_{1H'}$ about its minimum. The value of $\chi^2_{1H'}$ on the ellipses evaluated in the quadratic limit is ${}_{95}\chi^2_{(2)}$ = 14.3. The dashed red contour levels with $\chi^2_{1H'}$ = 14.3 represent the estimates of the 95% confidence regions for parameters derived from the 1H' model

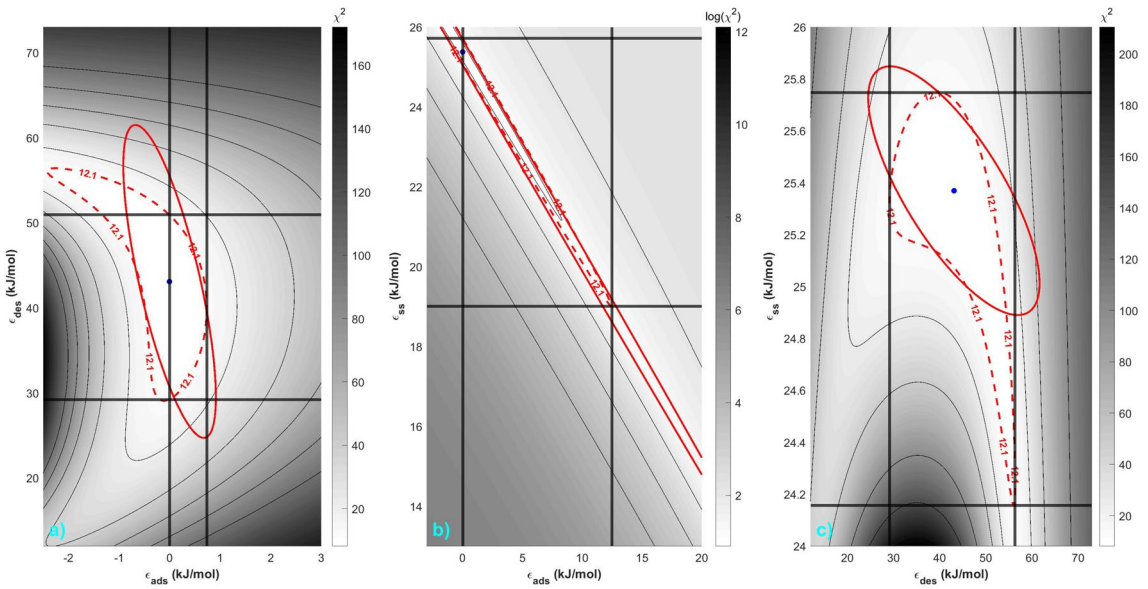

Fig. 14 Grayscale contour plots of **a** $\chi^2_{2H'}(\epsilon_{ads}, \epsilon_{des})$ with ΔE_{ss} = 25 kJ/mol, **b** $\log(\chi^2_{2H'}(\epsilon_{ads}, \epsilon_{ss}))$ with $\Delta E^{\ddagger}_{des}$ = 43 kJ/mol, and c) $\chi^2_{2H'}(\epsilon_{des}, \epsilon_{ss})$ with $\Delta E^{\ddagger}_{ads}$ = 0 given by the 2H' model for H_2–D_2 exchange on Pd. In all three plots, the blue dot marks the global minimum found at $\Delta E^{\ddagger}_{ads}$ = 0, $\Delta E^{\ddagger}_{des}$ = 43.1 kJ/mol, and ΔE_{ss} = 25.4 kJ/mol with χ^2_{min} = 8.2. The red error ellipses represent the 95% confidence limit assuming a quadratic form for $\chi^2_{2H'}$ about its minimum. The value of $\chi^2_{2H'}$ on the ellipses evaluated in the quadratic limit is ${}_{95}\chi^2_{(2)}$ = 12.1. The dashed red contour levels with $\chi^2_{2H'}$ = 12.1 represent the estimates of the 95% confidence regions for parameters derived from the 2H' model

Table 1 Summary of the fitting results for the Pd catalyst

	Langmuir–Hinshelwood (LH)	Single subsurface hydrogen (1H')	Dual subsurface hydrogen (2H')
$\Delta E^{\ddagger}_{ads}$(kJ/mol)	51.1	0	0
95% conf. bounds	50.6–51.7	0 – 6	0–12
$\Delta E^{\ddagger}_{des}$(kJ/mol)	–	20	43
95% conf. bounds	–	13–29	29–56
ΔE_{ss}(kJ/mol)	–	46	25
95% conf. bounds	–	40–47	19–26
χ^2_{min}	6.4	10.4	8.2
${}_{95}\chi^2_{(2)}$	9.4	14.3	12.1

parameters for each reaction mechanism are presented in Table 1.

6 Evaluation of Model Performance and Fitting Methodology

The goal of fitting three different mechanistic models to the kinetic data for H_2–D_2 exchange on Pd is to identify the one that best describes the data and best represents the real mechanism. A thorough implementation of parameter and uncertainty estimation has yielded the kinetic parameters and their 95% confidence intervals presented in Table 1. Since the parameter values for $\Delta E^{\ddagger}_{ads}$, $\Delta E^{\ddagger}_{des}$, and ΔE_{ss} have physical significance, analysis of the fitting results can yield important insight into the physical possibility of the associated mechanism.

At first glance, it is difficult to distinguish between the quality of the optimal solutions found for each mechanism. The red, green, and blue curves in Fig. 11 illustrate the predictions of $F^{out}_{HD}(T;P_{H_2},P_{D_2})$ by the best fits of the LH, 1H′, and 2H′ models to the experimental data. They are nearly overlapping, and have comparable values of χ^2_{min}. In the case of the LH model, we can only report values for the adsorption energy barrier, $\Delta E^{\ddagger}_{ads}$, because χ^2 is insensitive to $\Delta E^{\ddagger}_{des}$ in this regime. The LH mechanism predicts $\Delta E^{\ddagger}_{ads} = 51.1 \pm 0.6$ kJ/mol with 95% confidence. However, this is unrealistic for a Pd catalyst, which is known to have a negligible energy barrier for H_2 dissociation [28–30]. In addition, the LH model is unable to account for the zero-order dependence of the reaction rate on P_{H_2} under conditions where $P_{H_2} \gg P_{D_2}$ and $\theta \approx 1$, as reported previously [33]. Thus, in spite of its low value of χ^2 the LH mechanism cannot account for the observed kinetics for H_2–D_2 exchange using physically reasonable kinetic parameters. In contrast, both subsurface models predict $\Delta E^{\ddagger}_{ads} = 0$ for their best fit solutions, and the 2H′ mechanism supports the observation that $n_{H_2} = 0$ under experimental conditions with $P_{H_2} \gg P_{D_2}$ [33]. Therefore, these fitting results provide additional evidence that H_2–D_2 exchange follows non-LH kinetics.

We can also calculate the adsorption energy for hydrogen, $\Delta E_{ads} = \Delta E^{\ddagger}_{ads} - \Delta E^{\ddagger}_{des}$, predicted by the most probable values of $\Delta E^{\ddagger}_{ads}$ and $\Delta E^{\ddagger}_{des}$ for each model. While we do not report a value for $\Delta E^{\ddagger}_{des}$ using the LH model, it is clear from Fig. 12 that the mechanism predicts $\Delta E_{ads} > 0$ since $\Delta E^{\ddagger}_{ads} > \Delta E^{\ddagger}_{des}$ within the entire 95% confidence region. By contrast, the 1H′ and 2H′ mechanisms predict $\Delta E_{ads} = -20$ kJ/mol and $\Delta E_{ads} = -43$ kJ/mol, respectively, which is consistent with the understanding that dissociative hydrogen adsorption is exothermic. DFT calculations have found that $\Delta E_{ads} = -101$ kJ/mol for H_2 on Pd (100) and that $\Delta E_{ads} = -114$ kJ/mol for H_2 on Pd (111) [29]. Experimental studies have measured the hydrogen adsorption energy to be systematically lower than DFT predictions, $\Delta E_{ads} = -87$ kJ/mol for Pd (100) [28], and $\Delta E_{ads} = -99$ kJ/mol for Pd(111) [45]. The predictions of the 2H′ mechanism are in better agreement with the expectations for ΔE_{ads} from the literature.

While both subsurface models predict the same value for $\Delta E^{\ddagger}_{ads}$, they have different implications for $\Delta E^{\ddagger}_{des}$ and ΔE_{ss}. For the 2H′ mechanism, $\Delta E^{\ddagger}_{des} > \Delta E_{ss}$, which means that the equilibrium constant for surface-subsurface diffusion, K_{ss}, is less sensitive to temperature changes than the desorption rate constant, k_{des}. The opposite is true for the 1H′ mechanism, where $\Delta E^{\ddagger}_{des} < \Delta E_{ss}$. This difference highlights the fundamental preference of the 2H′ mechanism for populating the subsurface in order to facilitate the adsorption and desorption processes. The value of $\Delta E_{ss} = 25$ kJ/mol predicted by the 2H′ mechanism for Pd is consistent with a DFT study by Ferrin et al. who calculated the surface–subsurface energy difference for hydrogen atoms on various transition metal single crystals [29]. In their work, $\Delta E_{ss} = 29$ kJ/mol for Pd(111) and $\Delta E_{ss} = 30$ kJ/mol for Pd(100), similar to the value predicted by the 2H′ mechanism. Finally, the 2H′ mechanism predicts $\Delta E^{\ddagger}_{ads} = 0$ consistent with values measured on clean Pd surfaces [28–30], and predicts $n_{H_2} = 0$ under the experimental conditions at which this is observed. As such, the 2H′ model is the most consistent with the current understanding of H_2–D_2 exchange kinetics.

7 Conclusion

This work presented the methodology for kinetic parameter estimation from reaction data and for estimating the confidence regions associated with these parameters. In particular, we have illustrated the difficulty in independently estimating the values of ν and $\Delta E^{\ddagger}$ associated with

Arrhenius-like rate constants. The best practice uses transition state theory to constrain the values of the pre-exponential factor before then estimating the value of the energy barrier. Numerical solvers can encounter pitfalls, such as the presence of multiple solutions and regions of parameter space where the sum of squared errors (χ^2) is insensitive to parameter values. These issues can render it impossible to quantify such parameters with useful accuracy. For this reason, it is essential to investigate the local environment around a suspected global minimum of χ^2 to quantify the degree of (un)certainty in the solver output. Error ellipses can be used to visualize the bivariate relationships between pairs of parameters around the global minimum in multidimensional parameter space. Since the models had non-Gaussian distributions of error in χ^2, the error ellipses bounding the 95% confidence region were converted into contours of constant $\chi^2 = {}_{95}\chi^2_{(2)}$ determined by a quadratic approximation to χ^2. The extrema of these contours can be interpreted as conservative estimates for the 95% confidence limits of the kinetic parameters.

Using the above methodology, three different mechanistic models, LH, 1H′, and 2H′, were fit to the H_2–D_2 exchange activity of a Pd catalyst. In fitting the models to the reaction data, we obtained estimates for the fundamental energetics describing hydrogen adsorption, desorption, and surface-to-subsurface diffusion. While all three mechanisms fit the data with a similar value of χ^2_{min}, the kinetic parameters predicted at the global minima varied significantly. The LH model was only capable of estimating $\Delta E^{\ddagger}_{ads} = 51.1 \pm 0.6$ kJ/mol, which disagrees with the literature for H_2 adsorption on Pd. Both subsurface models predicted $\Delta E^{\ddagger}_{ads} = 0$, but only the 2H′ mechanism was also able to match the DFT prediction for ΔE_{ss} and the experimental observation of the reaction order in P_{H_2} of $n_{H_2} = 0$ for conditions where $P_{H_2} \gg P_{D_2}$. Ultimately, the estimates for $\Delta E^{\ddagger}_{ads}$, $\Delta E^{\ddagger}_{des}$, and ΔE_{ss} and inclusion of the uncertainty on each parameter give additional insight into the mechanism for H_2–D_2 exchange on Pd.

Acknowledgements The authors would like to acknowledge financial support for this work from the National Science Foundation through grant number CHE1954340.

Declarations

Conflicts of interest The authors have no conflict of interest.

References

1. Strasser P, Fan Q, Devenney M, Weinberg WH, Liu P, Nørskov JK (2003) High throughput experimental and theoretical predictive screening of materials—a comparative study of search strategies for new fuel cell anode catalysts. J Phys Chem B. https://doi.org/10.1021/jp030508z
2. Reddington E, Sapienza A, Gurau B, Viswanathan R, Sarangapani S, Smotkin ES, Mallouk TE (1998) Combinatorial electrochemistry: a highly parallel, optical screening method for discovery of better electrocatalysts. Science. https://doi.org/10.1126/science.280.5370.1735
3. Smotkin ES, Jiang J, Nayar A, Liu R (2006) High-throughput screening of fuel cell electrocatalysts. Appl Surf Sci. https://doi.org/10.1016/j.apsusc.2005.08.115
4. Satyapal S (2015) DOE hydrogen and fuel cells program, FY2015 annual progress report. DOE Hydrog. Fuel Cells Program, FY2015 Annu. Prog. Report, Introd
5. Gmeiner J, Seibicke M, Behrens S, Spliethoff B, Trapp O (2016) Investigation of the hydrogenation of 5-methylfurfural by noble metal nanoparticles in a microcapillary reactor. Chemsuschem. https://doi.org/10.1002/cssc.201600045
6. Shevlin M, Friedfeld MR, Sheng H, Pierson NA, Hoyt JM, Campeau LC, Chirik PJ (2016) Nickel-catalyzed asymmetric alkene hydrogenation of α, β-unsaturated esters: high-throughput experimentation-enabled reaction discovery, optimization, and mechanistic elucidation. J Am Chem Soc. https://doi.org/10.1021/jacs.6b00519
7. Pizzi R, van Putten RJ, Brust H, Perathoner S, Centi G, van der Waal JC (2015) High-throughput screening of heterogeneous catalysts for the conversion of furfural to bio-based fuel components. Catalysts. https://doi.org/10.3390/catal5042244
8. Gmeiner J, Behrens S, Spliethoff B, Trapp O (2016) Ruthenium nanoparticles in high-throughput studies of chemoselective carbonyl hydrogenation reactions. ChemCatChem. https://doi.org/10.1002/cctc.201501069
9. Adhikari S, Fernando S (2006) Hydrogen membrane separation techniques. Ind Eng Chem Res. https://doi.org/10.1021/ie050644l
10. Lanning BR, Ishteiwy O, Way JD, Edlund D, Coulter K (2009) Un-Supported palladium alloy membranes for the production of hydrogen. Inorganic Membranes Energy Environ Appl. https://doi.org/10.1007/978-0-387-34526-0_11
11. Paglieri SN, Way JD (2002) Innovations in palladium membrane research. Sep Purif Methods. https://doi.org/10.1081/SPM-120006115
12. Hammer B, Norskov JK (1995) Why gold is the noblest of all the metals. Nature. https://doi.org/10.1038/376238a0
13. Aasberg-Petersen K, Nielsen CS, Lægsgaard Jørgensen S (1998) Membrane reforming for hydrogen. Catal Today. https://doi.org/10.1016/S0920-5861(98)00341-1
14. deRosset AJ (1960) Diffusion of hydrogen through palladium membranes. Ind Eng Chem. https://doi.org/10.1021/ie50606a035
15. Sinfelt JH, Catal CJ, Catal, AE (1987) Bimetallic catalysts: discoveries, concepts, and applications
16. Wei T, Wang J, Goodman DW (2007) Characterization and chemical properties of Pd-Au alloy surfaces. J Phys Chem C. https://doi.org/10.1021/jp067177l
17. Lewis FA (1995) The palladium-hydrogen system: structures near phase transition and critical points. Int J Hydrogen Energy. https://doi.org/10.1016/0360-3199(94)00113-E
18. Jayaraman V, Lin YS (1995) Synthesis and hydrogen permeation properties of ultrathin palladium-silver alloy membranes. J Memb Sci. https://doi.org/10.1016/0376-7388(95)00040-J
19. Shu J, Grandjean BPA, Neste A, Van Kaliaguine S (1991) Catalytic palladium-based membrane reactors: a review. Can J Chem Eng. https://doi.org/10.1002/cjce.5450690503
20. Rogers HC (1968) Hydrogen embrittlement of metals: atomic hydrogen from a variety of sources reduces the ductility of many metals. Science. https://doi.org/10.1126/science.159.3819.1057

21. OBrien CP, Miller JB, Morreale BD, Gellman AJ (2011) The kinetics of H 2-D 2 exchange over Pd, Cu, and PdCu surfaces. J Phys Chem. https://doi.org/10.1021/jp2076885
22. O'Brien CP, Miller JB, Morreale BD, Gellman AJ (2012) H_2–D_2 exchange kinetics in the presence of H_2S over Pd_4S, $Pd_{70}Cu_{30}$, and $Pd_{47}Cu_{53}$ surfaces. J Phys Chem C. https://doi.org/10.1021/jp305024b
23. Lewis FA (1982) Palladium-hydrogen system - 2. Platin Met Rev
24. Uemiya S, Matsuda T, Kikuchi E (1991) Hydrogen permeable palladium-silver alloy membrane supported on porous ceramics. J Memb Sci. https://doi.org/10.1016/S0376-7388(00)83041-0
25. Hurlbert RC, Konecny JO (1961) Diffusion of hydrogen through palladium. J Chem Phys. https://doi.org/10.1063/1.1701003
26. Jewett DN, Makrides AC (1965) Diffusion of hydrogen through palladium and palladium-silver alloys. Trans Faraday Soc. https://doi.org/10.1039/tf9656100932
27. Pyun S, Lee WT, Yang TH (1997) Hydrogen diffusion through palladium-gold alloy coatings electrodeposited on palladium substrate under permeable boundary condition. Thin Solid Films. https://doi.org/10.1016/S0040-6090(97)00458-6
28. Conrad H, Ertl G, Latta EE (1974) Adsorption of hydrogen on palladium single crystal surfaces. Surf Sci. https://doi.org/10.1016/0039-6028(74)90060-0
29. Ferrin P, Kandoi S, Nilekar AU, Mavrikakis M (2012) Hydrogen adsorption, absorption and diffusion on and in transition metal surfaces: a DFT study. Surf Sci. https://doi.org/10.1016/j.susc.2011.12.017
30. Herron JA, Tonelli S, Mavrikakis M (2012) Atomic and molecular adsorption on Pd(111). Surf Sci. https://doi.org/10.1016/j.susc.2012.07.003
31. Ludwig W, Savara A, Madix RJ, Schauermann S, Freund HJ (2012) Subsurface hydrogen diffusion into Pd nanoparticles: role of low-coordinated surface sites and facilitation by carbon. J Phys Chem C. https://doi.org/10.1021/jp209033s
32. Savara A, Ludwig W, Schauermann S (2013) Kinetic evidence for a non-langmuir-hinshelwood surface reaction: H/D exchange over Pd nanoparticles and Pd(111). ChemPhysChem. https://doi.org/10.1002/cphc.201300179
33. Sen I, Gellman AJ (2018) Kinetic fingerprints of catalysis by subsurface hydrogen. ACS Catal. https://doi.org/10.1021/acscatal.8b02168
34. Teschner D, Borsodi J, Wootsch A, Révay Z, Hävecker M, Knop-Gericke A, Jackson SD, Schlögl R (2008) The roles of subsurface carbon and hydrogen in palladium-catalyzed alkyne hydrogenation. Science. https://doi.org/10.1126/science.1155200
35. Khan NA, Shaikhutdinov S, Freund HJ (2006) Acetylene and ethylene hydrogenation on alumina supported Pd-Ag model catalysts. Catal Lett. https://doi.org/10.1007/s10562-006-0041-y
36. Greeley J, Mavrikakis M (2005) Surface and subsurface hydrogen: adsorption properties on transition metals and near-surface alloys. J Phys Chem B. https://doi.org/10.1021/jp046540q
37. Mei D, Neurock M, Smith CM (2009) Hydrogenation of acetylene-ethylene mixtures over Pd and Pd-Ag alloys: first-principles-based kinetic monte carlo simulations. J Catal. https://doi.org/10.1016/j.jcat.2009.09.004
38. Studt F, Abild-Pedersen F, Bligaard T, Sørensen RZ, Christensen CH, Nørskov JK (2008) On the role of surface modifications of palladium catalysts in the selective hydrogenation of acetylene. Angew Chemie - Int Ed. https://doi.org/10.1002/anie.200802844
39. Christmann K (1988) Interaction of hydrogen with solid surfaces. Surf Sci Rep. https://doi.org/10.1016/0167-5729(88)90009-X
40. Kondratyuk P, Gumuslu G, Shukla S, Miller JB, Morreale BD, Gellman AJ (2013) A microreactor array for spatially resolved measurement of catalytic activity for high-throughput catalysis science. J Catal. https://doi.org/10.1016/j.jcat.2012.12.015
41. Fleutot B, Miller JB, Gellman AJ (2012) Apparatus for deposition of composition spread alloy films: the rotatable shadow mask. J Vac Sci Technol A Vacuum Surfaces Film. https://doi.org/10.1116/1.4766194
42. Catalytic Reaction Engineering. Stud Surf Sci Catal 1993 79(C): 251–306. https://doi.org/10.1016/S0167-2991(08)63811-2.
43. Dumesic JA (1993) The microkinetics of heterogeneous catalysis. ACS Prof Ref B
44. Wang B, Shi W, Miao Z (2015) Confidence analysis of standard deviational ellipse and its extension into higher dimensional euclidean space. PLoS ONE. https://doi.org/10.1371/journal.pone.0118537
45. Behm RJ, Christmann K, Ertl G (1980) Adsorption of hydrogen on Pd(100). Surf Sci 99(2):320–340. https://doi.org/10.1016/0039-6028(80)90396-9